AD______________

Award Number: W81XWH-09-1-0113

TITLE: INVESTIGATION OF ANTIANGIOGENIC MECHANISMS USING NOVEL IMAGING TECHNIQUES

PRINCIPAL INVESTIGATOR: ANDREW FONTANELLA

CONTRACTING ORGANIZATION: Duke University
Durham, NC 27706

REPORT DATE: February 2011

TYPE OF REPORT: Annual Summary

PREPARED FOR: U.S. Army Medical Research and Materiel Command
Fort Detrick, Maryland 21702-5012

DISTRIBUTION STATEMENT: Approved for public release; distribution unlimited

REPORT DOCUMENTATION PAGE	*Form Approved* *OMB No. 0704-0188*

1. REPORT DATE *(DD-MM-YYYY)* 01-02-2011	**2. REPORT TYPE** Annual Summary	**3. DATES COVERED** *(From - To)* 1 Feb 2010 - 31 Jan 2011

4. TITLE AND SUBTITLE INVESTIGATION OF ANTIANGIOGENIC MECHANISMS USING NOVEL IMAGING TECHNIQUES	**5a. CONTRACT NUMBER**
	5b. GRANT NUMBER W81XWH-09-1-0113
	5c. PROGRAM ELEMENT NUMBER
6. AUTHOR(S) ANDREW FONTANELLA E-Mail: andrew.fontanella@duke.edu	**5d. PROJECT NUMBER**
	5e. TASK NUMBER
	5f. WORK UNIT NUMBER
7. PERFORMING ORGANIZATION NAME(S) AND ADDRESS(ES) Duke University Durham, NC 27706	**8. PERFORMING ORGANIZATION REPORT NUMBER**
9. SPONSORING / MONITORING AGENCY NAME(S) AND ADDRESS(ES) U.S. Army Medical Research and Materiel Command Fort Detrick, Maryland 21702-5012	**10. SPONSOR/MONITOR'S ACRONYM(S)**
	11. SPONSOR/MONITOR'S REPORT NUMBER(S)

12. DISTRIBUTION / AVAILABILITY STATEMENT

Approved for Public Release; Distribution Unlimited

13. SUPPLEMENTARY NOTES

14. ABSTRACT

Abstract on next page.

15. SUBJECT TERMS

Angiogenesis, Optical Techniques, Tumor Pathophysiology, Treatment Response, Vascular Normalization

16. SECURITY CLASSIFICATION OF:			**17. LIMITATION OF ABSTRACT**	**18. NUMBER OF PAGES**	**19a. NAME OF RESPONSIBLE PERSON** USAMRMC
a. REPORT U	**b. ABSTRACT** U	**c. THIS PAGE** U	UU	35	**19b. TELEPHONE NUMBER** *(include area code)*

14. ABSTRACT

This study is intended to investigate the physiological effects of anti-angiogenic and anti-tumor treatment at the microcirculatory level with the intent to better understand how the tumor adapts to these treatments, with the aim of formulating more effective treatment modalities based off this knowledge. We have recently had the opportunity to form a collaboration with a research group investigating the effects of microbeam radiation therapy (MRT). Previous studies have shown that MRT induces a strong anti-tumor effect while sparing normal tissue. The mechanisms of this tissue-sparing effect are poorly understood, however. Investigation of MRT in the murine window chamber model will not only elucidate the mechanisms of MRT, but will also provide further insight into natural tumor progression and how the tumor may respond to vascular disrupting agents in general. We have employed a number of advanced techniques in the window chamber model to optically observe natural and induced changes in tumor physiology. These advanced imaging modalities have the advantage of being able to facilitate longitudinal, in vivo investigation into the parameters of interest. These include *Doppler Optical Coherence Tomography* for the measurement of blood flow velocity, *Hyperspectral Imaging* for the measurement of hemoglobin saturation and hematocrit, and *Confocal Imaging* for the measurement of 3-D vascular architecture and perfusion. Additionally, novel methods have been developed to molecularly probe the tumor environment. These include *Oxygen Sensitive Nanoparticles* for the mapping of pO2 and the use of *Engineered Cell Lines* which express green fluorescent protein under hypoxia. Together, these techniques will allow us to better understand and model the process of tumor growth and response to MRT, eventually leading to a better understanding of how such changes can be exploited to increase the efficacy of combinational therapies.

Table of Contents

Page

Introduction……………………………………………………………..………..….. **4**

Body…………………………………………………………………………….. **4**

Key Research Accomplishments……………………………………….…….. **10**

Reportable Outcomes……………………………………………………………… **10**

Conclusion…………………………………………………………………………. **11**

References……………………………………………………………………………. **11**

Appendices…………………………………………………………………………. **11**

Supporting Data……………………………………………………………………. **11**

INTRODUCTION:

This study is intended to investigate the physiological effects of anti-angiogenic and anti-tumor treatment at the microcirculatory level with the intent to better understand how the tumor adapts to these treatments, with the aim of formulating more effective treatment modalities based off this knowledge. We have recently had the opportunity to form a collaboration with a research group investigating the effects of microbeam radiation therapy (MRT). Previous studies have shown that MRT induces a strong anti-tumor effect while sparing normal tissue. The mechanisms of this tissue-sparing effect are poorly understood, however. Investigation of MRT in the murine window chamber model will not only elucidate the mechanisms of MRT, but will also provide further insight into natural tumor progression and how the tumor may respond to vascular disrupting agents in general. We have employed a number of advanced techniques in the window chamber model to optically observe natural and induced changes in tumor physiology. These advanced imaging modalities have the advantage of being able to facilitate longitudinal, in vivo investigation into the parameters of interest. These include *Doppler Optical Coherence Tomography* for the measurement of blood flow velocity, *Hyperspectral Imaging* for the measurement of hemoglobin saturation and hematocrit, and *Confocal Imaging* for the measurement of 3-D vascular architecture and perfusion. Additionally, novel methods have been developed to molecularly probe the tumor environment. These include *Oxygen Sensitive Nanoparticles* for the mapping of pO2 and the use of *Engineered Cell Lines* which express green fluorescent protein under hypoxia. Together, these techniques will allow us to better understand and model the process of tumor growth and response to MRT, eventually leading to a better understanding of how such changes can be exploited to increase the efficacy of combinational therapies.

BODY:

The grant application's Statement of Work listed a number of goals within Task 1 to be completed within the first 16 months of work. These goals largely consisted of the development and refinement of imaging modalities for the optical interrogation of tumors grown in a window chamber. While the essence of this project has remained consistent, we have elected to employ the dorsal window chamber model (rather than the mammary window chamber model) for the initial stages of the project. While the mammary window chamber model has the advantage of allowing for orthotopic tumor implantation, we felt that the benefits of the dorsal model outweighed this advantage. The ability to use trans-illumination to image the dorsal window chamber provides more accurate results when using the hyperspectral imaging technique, as it does not require complicated modeling of depth-dependant tissue reflectance and scattering. Additionally, many of the imaging modalities would require significant modification to facilitate the mammary model. For our initial investigation into unmodulated tumor progression, we felt that the dorsal model would provide cleaner, more easily processed data that would eventually facilitate adaptation to the mammary model, once basic modulations of physiological parameters were thoroughly modeled and understood.

Since submission of the last annual report, we have made significant refinements to the image processing algorithms used to automatically quantify vascular parameters. These algorithms constitute an invaluable tool by which we are capable of quickly and objectively quantifying induced changes in vascular structure and functionality. Variables that this algorithm is capable of quantifying include vascular length density, total branchpoints, tortuosity, and vascular diameter. Additionally, we have developed code that is able to process video-rate sequences of blood flow images and provide quantitative maps of flow direction and velocity. This advancement (in conjunction with other techniques for measuring hemoglobin saturation and HIF-1 expression) is particularly useful in helping us to understand how blood-flow patterns affect the local tumor microenvironment. We expect to publish data derived from this algorithm within the next few months.

The recent development of oxygen sensitive nanoparticles through collaboration with Cassandra Fraser at the University of Virginia has provided us with an additional technique for optically measuring extravascular pO_2[1]. We have already employed this tool in a preliminary study of oxygen transport and hemodynamics. We will continue to employ these nanoparticles throughout the rest of this study.

Finally, we wish to report an exciting opportunity that had arisen soon after the submission of the last annual report. We have been provided with the opportunity to collaborate with a group at the University of North Carolina – Chapel Hill that is studying the effects of microbeam radiation therapy. Microbeam radiation therapy (MRT) is a unique form of radiotherapy that has shown a marked tumor-specific effect. Compared to conventional radiation forms, MRT produces microscopic, spatially-discrete radiation patterns at an ultrahigh dose rate. The tissue-sparing property of this unique treatment modality is possibly facilitated by efficient normal vessel repair mechanisms, contrary to the catastrophic disruption of poorly regulated tumor-associated vasculature. However, the non-local response characteristics associated with this treatment are not clearly understood. Therefore, we have begun work to investigate this treatment in the window chamber model in order to observe and spatially quantify treatment response in terms of modulation of vascular structure and functionality. In a preliminary study, over a week-long time course, we observed induced changes in tumor-associated vasculature after the MRT treatment. Time course images and analysis presented here suggest a treatment-induced modulation of the tumor vasculature with regard to both structure and function. We will continue this work throughout the next year, employing all of the automated image processing techniques that were described previously. We expect that this data will yield invaluable information on how MRT is able to specifically target the tumor. Furthermore, it will provide additional information on how tumor vasculature naturally adapts its vascular delivery line to compensate for inefficiencies in function do to poorly regulated angiogenesis. Beyond investigation of the effects of MRT, these data will provide insight into the mechanisms and shortcomings of traditional anti-vascular treatments.

Below are presented the tasks originally proposed to be completed in the first 16 months of the project, along with discussions of accomplishments or alterations to these tasks:

SOW – Task 1a: *Learn mammary window chamber surgical technique (month 1-2)*

As discussed above, we have decided to employ dorsal window chamber and fiber probe based techniques, rather than the mammary window chamber procedure. I have since become proficient at both of these techniques and have applied them in a number of preliminary studies.

> **SOW – Task 1b**: *Establish method for extracting fluorescein concentrations in extravascular space using published data by Dr. Gregory Palmer. Palmer will provide guidance. (month 1-2)*

This method has been established and will be employed in future drug kinetics studies.

> **SOW – Task 1c**: *Hemoglobin saturation extraction software will need to be adapted to mammary window chamber measurements. (month 1-2)*

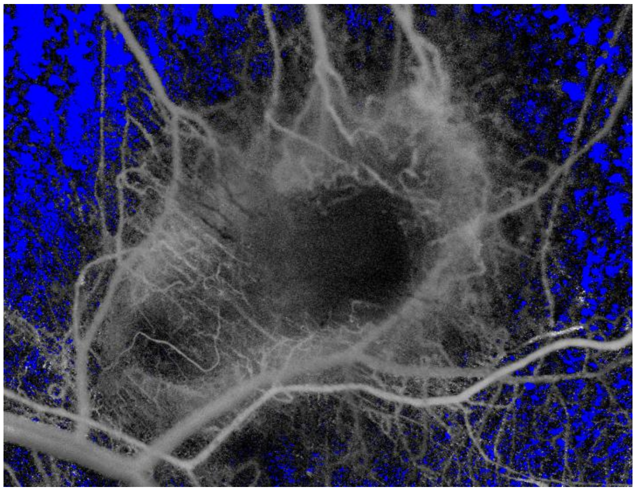

Figure 1, showing the original hemoglobin saturation reconstruction: Hemoglobin saturation is represented as grayscale values, independent of total hemoglobin content within the vessels. This representation has the drawback of not being able to represent important variations in individual vessels' hemoglobin (and thus oxygen) delivering capacity.

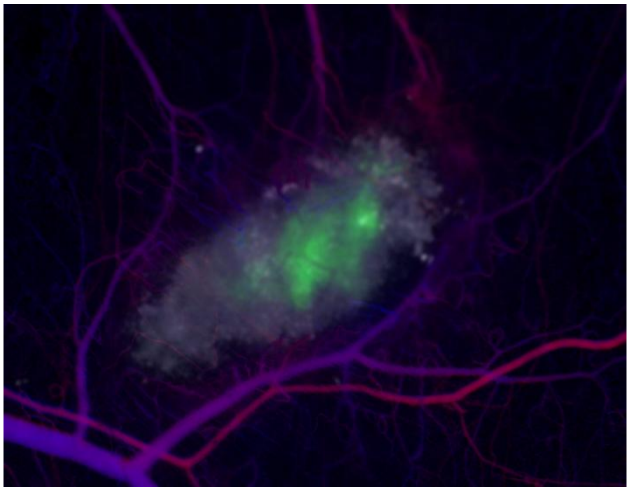

Figure 2, showing the same tumor, but incorporating improvements made to the hyperspectral processing algorithm: Total hemoglobin is factored into the new algorithm and is represented as vascular brightness. Hemoglobin saturation is represented on a blue-red color axis, with blue and red representing fully deoxygenated and oxygenated blood, respectively. The tumor appears in white, while hypoxia-indicating GFP is represented by its green intensity within the tumor.

Since the dorsal window chamber has replaced the mammary window chamber in this aim of the study, no physical modifications to the hyperspectral system were necessary. I have, however, made improvements to the computational reconstruction algorithm (Figs 1&2), and we are now able to extract total hemoglobin values from our data. Total hemoglobin will be incorporated into all of our window chamber studies from this point forward.

> **SOW – Task 1d**: *Practice imaging modalities and collect preliminary data. (month 3)*

This task has been completed and has progressed towards the more detailed analysis of Task 1e.

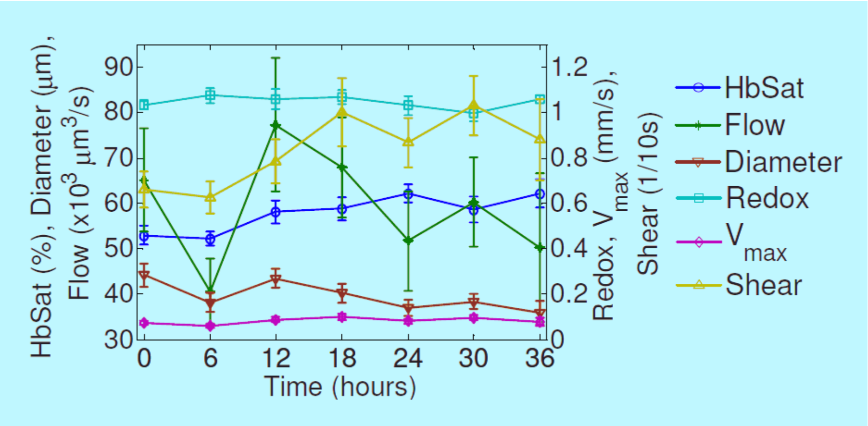

Figure 3, showing recently published data regarding longitudinal variations in important physiological parameters over a 36 hour time course: Values at each time point were averaged across all regions of interest. Hemoglobin saturation, flow velocity, vessel diameter, redox ratio, maximum velocity, and shear rate were all shown to significantly change with time (p<0.05).

SOW – Task 1e: *Collect HIF-1, hemoglobin saturation, red blood cell flux, drug delivery, and vascular structure data for SA1. (month 4-15)*

These parameters (minus the HIF-1 reporter), along with redox ratio, were investigated in two recent papers[2-3]. HIF-1 (as reported by GFP) presented an obstacle to obtaining accurate redox ratio values, as the GFP spectrum overlaps with and overpowers the weak FAD fluorescence signal (redox ratio is measured as the ratio of FAD to NADH). Since this particular timecourse investigated short term physiological changes (every 6 hours for 36 hours), we felt that redox ratio was a better parameter to track, since the long half-life of GFP might produce misleading quantities over such a short timeframe. The data that we collected yielded interesting correlations among all of these parameters (Fig 3). In a separate paper, the oxygen-sensitive nanoparticles were employed to investigate oxygenation and hemodynamic properties in tumors (Fig 4). This paper demonstrates interesting correlations between pO2 and vascular function, and will establish a model by which oxygen delivery to the tumor may be better understood.

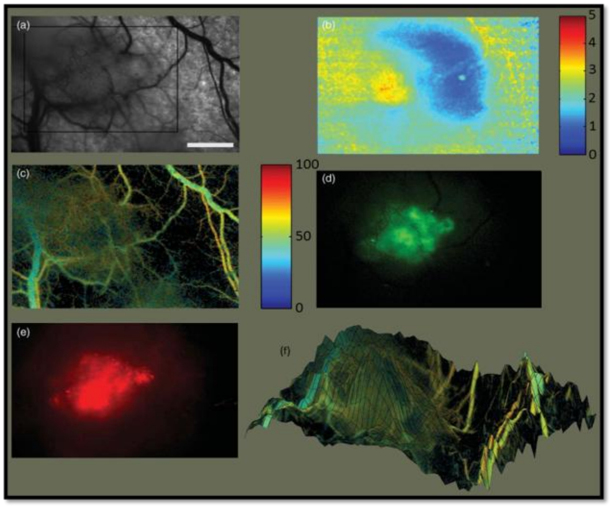

Figure 4: The data presented above are from a recently published study (Palmer *et al*, JBO 2010) in which oxygen sensitive nanoparticles probes were used to measure oxygen tension in within a tumor and surrounding tissue. The images show (a) the tumor (boxed) under bright field illumination, (b) oxygen tension in the percent of oxygen, (c) hemoglobin oxygen saturation, (d) GFP-HIF-1 fluorescence, and (e) constitutively expressed RFP fluorescence. The hemoglobin saturation (c) is shown with percent oxygen saturation on a color scale whose brightness is modulated by the total hemoglobin content (thus, well-vascularized regions appear brighter). A combined plot (f) shows the hemoglobin oxygen saturation projected onto a 3-D surface whose vertical displacement corresponds to increased tissue oxygenation. A 1mm scale bar is shown in (a).

SOW – Task 1f: *Perform statistical analysis on data and formulate combinational treatment schedules for future SAs. These results will be reviewed by a statistician. (month 15-16)*

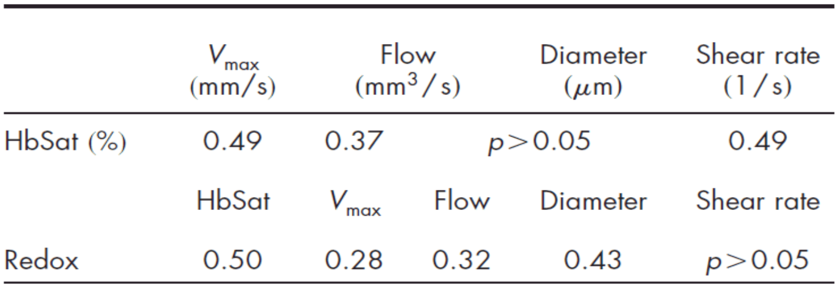

	V_{max} (mm/s)	Flow (mm^3/s)	Diameter (μm)	Shear rate (1/s)
HbSat (%)	0.49	0.37	$p > 0.05$	0.49

	HbSat	V_{max}	Flow	Diameter	Shear rate
Redox	0.50	0.28	0.32	0.43	$p > 0.05$

Figure 5, showing published statistical analysis of observed parameters: Results indicated a positive correlation between blood flow, hemoglobin saturation, and metabolic demand in tumors. But correlations are weak, suggesting no single biomarker can fully explain the behavior of another, and further highlighting the need for sophisticated models of tumor growth and adaptation.

The project has progressed significantly ahead of schedule with regard to this particular task. We have already performed some statistical analysis on our observations, and these results were published in a recent article (Fig 5)^3. Furthermore, we have mostly finalized our advanced image processing algorisms for the automated segmentation and analysis of vascular architecture (Fig 6). The extraction of total hemoglobin content was one of the first products of this effort, and we are well on our way towards developing an all encompassing algorithm to quantify mean vessel density, tortuosity, and mean vascular diameter from our images. Such an algorithm will allow us to automatically extract

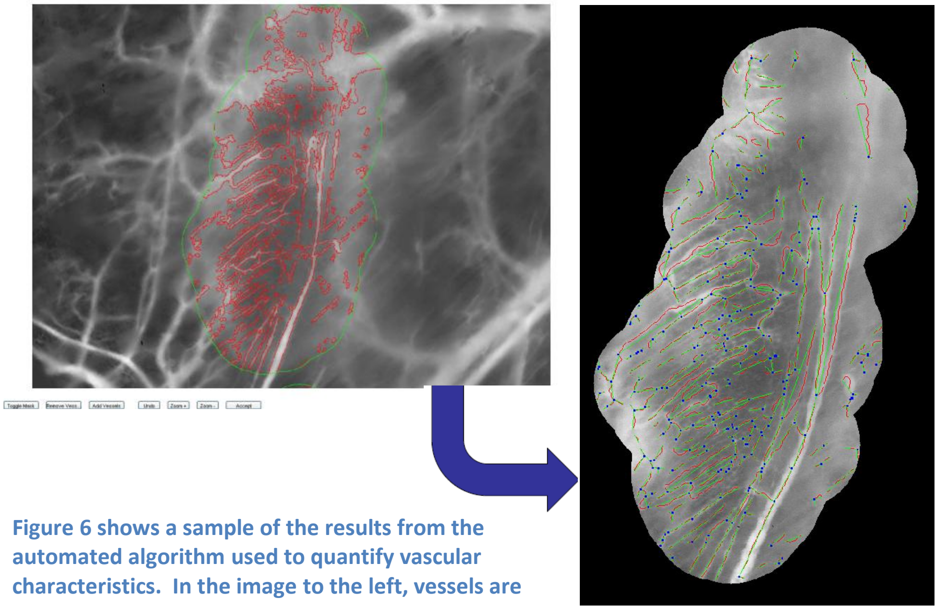

Figure 6 shows a sample of the results from the automated algorithm used to quantify vascular characteristics. In the image to the left, vessels are identified and highlighted in red within the region of interested identified by the green border. The right image shows the transformation of these vessel outline data into vascular parameters: Vessel centerlines are shown in red, while blue points show vessel branch points. The green lines represent straight-line distances between branch points, from which vessel tortuosity can be calculated. Vessel diameter and vascular length density can also be calculated from these data.

unbiased values for these parameters, circumventing the subjective and time-consuming task of performing manual image analysis.

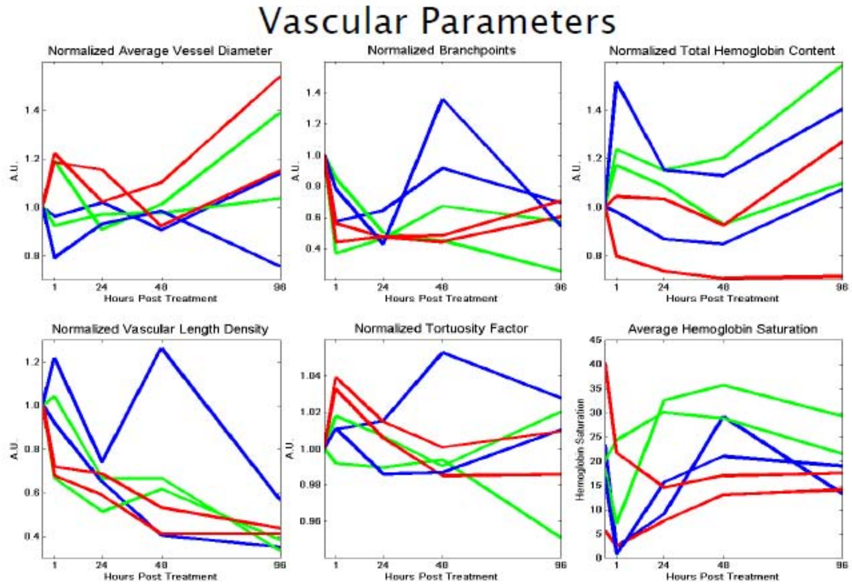

Figure 7 shows results from the automated algorithm used to quantify vascular characteristics. The blue lines represent changes in the low-dose microbeam animals over time. Widefield radiation and mock treatment controls are shown in red and green, respectively. While these preliminary results showed interesting qualitative trends and helped to validate the parameter quantification algorithms, actual values for these parameters yielded uncertain results. We expect to see more consistent and significant results with a larger number of high-dose treatments, however.

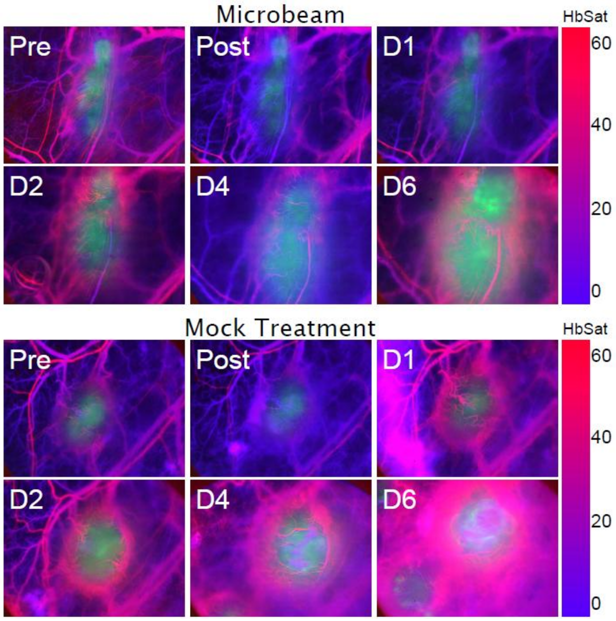

Figure 8 shows a sample of the hemoglobin saturation/HIF-1 images from the low-dose microbeam experiment. Hemoglobin saturation is representes as per the colorscale shown. HIF-1 expression (GFP) is represented in green. Low-dose treatment shows interesting qualitative results. Clearly there is an inhibition in tumor growth and vascular proliferation. These characteristics will be examined more thoroughly with the high-dose treatments.

SOW – Task 2a: *Collect HIF-1, hemoglobin saturation, red blood cell flux, drug delivery, and vascular structure data for SA 2 (17-26)*

As stated previously, focus on treatment investigation has shifted to microbeam radiation treatment. We have collected preliminary data investigating microbeam patterns at lower doses (approximately 10 Gy) (Fig 7 & 8), however, high-dose (> 25 Gy) treatments were delayed by technical difficulties with the microbeam generator. These issues were resolved in late 2010, and we have begun collecting data regarding this treatment.

KEY RESEARCH ACCOMPLISHMENTS:

- Developed appropriate animal protocols
- Improved hyperspectral analysis to extract total hemoglobin content
- Developed an algorithm for incorporating multiple physiological parameters into a single image for better visual analysis
- Developed methods for incorporating multiple imaging modalities into a single microscope system
- Collected data over a 36 hour time course which showed significant fluctuations in all physiological parameters over that timeframe
- Showed a statistically significant correlation among a number of physiological parameters, suggesting a multiparametric model of tumor progression is attainable
- Investigated hemodynamic properties of tumors and how these correspond to changes in oxygen delivery as assessed by oxygen-sensitive nanoparticles
- Developed an algorithm for quantification of blood flow velocity and direction in video-rate image sequences
- Performed preliminary investigation into low-dose microbeam radiation effects
- Began investigation of high-dose microbeam radiation effects

REPORTABLE OUTCOMES:

We have published three papers that demonstrate significant progress towards our goal of analyzing treatment-induced physiological changes and demonstrating refined understanding of treatment-induced effects upon vascular structure and function.

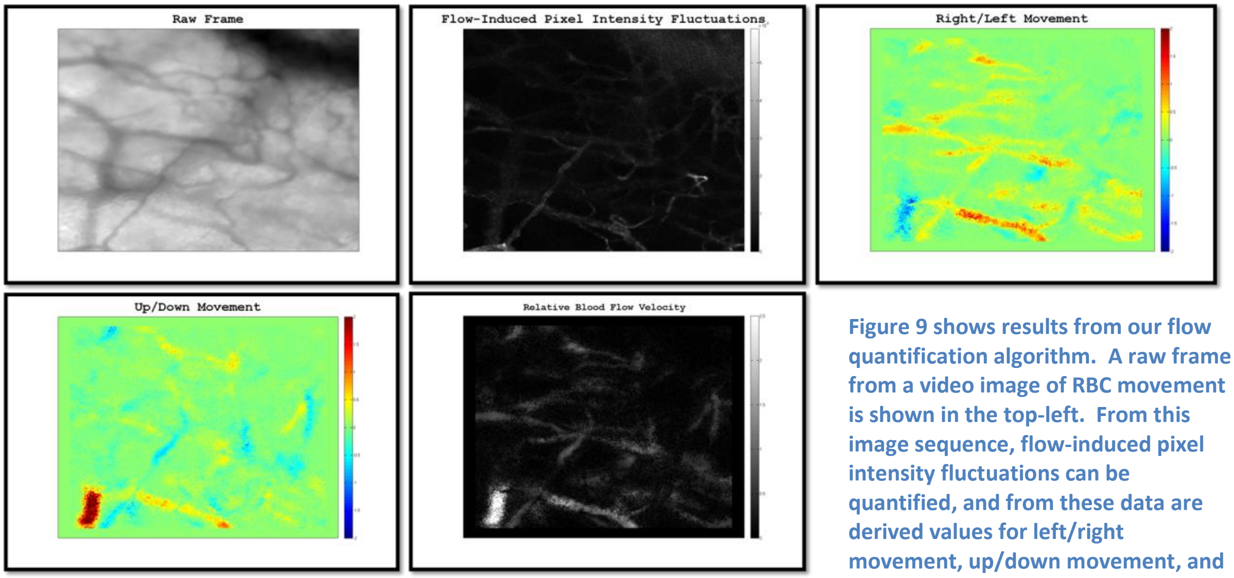

Figure 9 shows results from our flow quantification algorithm. A raw frame from a video image of RBC movement is shown in the top-left. From this image sequence, flow-induced pixel intensity fluctuations can be quantified, and from these data are derived values for left/right movement, up/down movement, and total velocity for every pixel in the video sequence.

CONCLUSION:

In the second year of work we have continued to develop optimized procedures for the analysis of key physiological parameters using optical methods. Our results from video analysis of red blood cell movement are particularly interesting (Fig 9), and we anticipate incorporating this analysis into our study and publishing this processing algorithm within the next few months. In addition to providing an invaluable tool for analysis of our data, we expect that this algorithm will find useful application in a number of instances of video analysis of hemodynamics by both our lab and others. We have begun investigation of the effects of microbeam radiation therapy on vascular function, and have already completed a preliminary analysis of low-dose treatments. These results provided and excellent model upon which to test our algorithms. We are now ready to proceed to a large scale investigation of MRT, and have recently begun a number of animal experiments.

REFERENCES:

1 Zhang, G., Palmer, G. M., Dewhirst, M. W. & Fraser, C. L. A dual-emissive-materials design concept enables tumour hypoxia imaging. *Nat Mater* 8, 747-751, doi:nmat2509 [pii] 10.1038/nmat2509 (2009).

2 Skala, M. C., Fontanella, A., Hendargo, H., Dewhirst, M. W. & Izatt, J. A. Combined hyperspectral and spectral domain optical coherence tomography microscope for noninvasive hemodynamic imaging. *Opt Lett* 34, 289-291, doi:176087 [pii] (2009).

3 Skala, M. C., Fontanella, A., Lan, L., Izatt, J. A. & Dewhirst, M. W. Longitudinal optical imaging of tumor metabolisam and hemodynamics. *J Biomed Opt* 15, 8 (2010).

4 Gregory M. Palmer, Andrew N. Fontanella, Guoqing Zhang, Gabi Hanna, Cassandra L. Fraser and Mark W. Dewhirst, "Optical imaging of tumor hypoxia dynamics", *J. Biomed. Opt.* 15, 066021 (Dec 20, 2010); doi:10.1117/1.3523363

APPENDICES:

Published articles derived from this work (References 2-4) are attached to the end of this document

SUPPORTING DATA:

Embedded within text

nature materials

LETTERS

| DOI: 10.1038/NMAT2509

A dual-emissive-materials design concept enables tumour hypoxia imaging

Guoqing Zhang[1], Gregory M. Palmer[2], Mark W. Dewhirst[2] and Cassandra L. Fraser[1]*

Luminescent materials are widely used for imaging and sensing owing to their high sensitivity, rapid response and facile detection by many optical technologies[1]. Typically materials must be chemically tailored to achieve intense, photostable fluorescence, oxygen-sensitive phosphorescence or dual emission for ratiometric sensing, often by blending two dyes in a matrix. Dual-emissive materials combining all of these features in one easily tunable molecular platform are desirable, but when fluorescence and phosphorescence originate from the same dye, it can be challenging to vary relative fluorescence/phosphorescence intensities for practical sensing applications. Heavy-atom substitution[2] alone increases phosphorescence by a given, not variable amount. Here, we report a strategy for modulating fluorescence/phosphorescence for a single-component, dual-emissive, iodide-substituted difluoroboron dibenzoylmethane-poly(lactic acid) (BF_2dbm(I)PLA) solid-state sensor material. This is accomplished through systematic variation of the PLA chain length in controlled solvent-free lactide polymerization[3] combined with heavy-atom substitution[2]. We demonstrate the versatility of this approach by showing that films made from low-molecular-weight BF_2dbm(I)PLA with weak fluorescence and strong phosphorescence are promising as 'turn on' sensors for aerodynamics applications[4], and that nanoparticles fabricated from a higher-molecular-weight polymer with balanced fluorescence and phosphorescence intensities serve as ratiometric tumour hypoxia imaging agents.

Ratiometric sensing addresses challenges associated with sensor concentration and obviates the need for specialized luminescence lifetime instrumentation. For example, Kopelman and co-workers developed a powerful nanosensor (PEEBLEs) for ratiometric oxygen sensing comprising a cyanine dye standard and an O_2-sensitive Pt porphyrin phosphor in a sol–gel matrix and demonstrated its utility for cell biology[5]. Single-component dye-polymer conjugates with both fluorescence and phosphorescence offer advantages over three-component dye/standard/matrix mixtures. Dual-emissive materials possess an internal rather than external standard in ratiometric sensing schemes, and thus, 1:1 fluorophore/phosphor stoichiometry, resulting in greater sample homogeneity and minimal dye leaching. Readily processable biomaterials combined with photostable, optically tunable dyes that emit brightly even in aqueous environments are beneficial for imaging and sensing in biomedical contexts.

Previously, we discovered that difluoroboron dibenzoylmethane-poly(lactic acid) (BF_2dbmPLA; as in Fig. 1, with hydrogen in place of iodide) exhibits unusual, long-lived green room-temperature phosphorescence (RTP) in addition to intense blue fluorescence[6]. Given that thermal decay pathways are often accessible, it is rare to see RTP from organic compounds; typically organized media[7,8] or heavy atoms[9] are required for RTP. This feature adds enhanced capability to the excellent fluorescence properties of boron dyes[10,11] and materials[12,13]. Nanoparticles fabricated from BF_2dbmPLA and related analogues show great promise for *in vitro* and *in vivo* imaging and oxygen sensing[14]. Although BF_2dbmPLA singlet and triplet emission are clearly distinguished on the basis of wavelength ($\lambda_F = 440$ nm, $\lambda_P = 509$ nm) and lifetime ($\tau_F = 2$ ns, $\tau_P = 170$ ms), the high singlet quantum yield ($\Phi_F \sim 0.80$) and much weaker RTP preclude the use of this first-generation material as a practical intensity-based ratiometric sensor. Ideally, much stronger phosphorescence intensity is required for ratiometric sensing. For insight into how to achieve this goal and modulate relative fluorescence to phosphorescence intensities, we turn to quantum theory.

According to perturbation theory, for a polyatomic molecule, the perturbation factor δ describing singlet–triplet mixing by first-order spin–orbit coupling can be expressed as in equation (1) (ref. 2),

$$\delta = \frac{\langle {}^3\Psi | H_{so} | {}^1\Psi \rangle}{|E_1 - E_3|} \tag{1}$$

where ${}^1\Psi$ and ${}^3\Psi$ are the wavefunctions of singlet and triplet states, respectively, H_{so} is the spin–orbit Hamiltonian and E_1 and E_3 are the energy levels for singlet and triplet states. This expression indicates that a greater spin–orbit matrix value and a smaller energy gap $|E_1 - E_3|$ correspond to a larger δ; that is, a high probability of electronic transition between singlet and triplet states. The spin–orbit matrix elements are highly sensitive to the atomic number of the atoms in the vicinity of the exciton. Heavy atoms either in the environment (external), or part of the luminescent molecule (internal) can enhance spin–orbit coupling and thus, increase the rate of intersystem crossing. Since the discovery of the internal heavy-atom effect by McClure[15] in 1949, halogens or large-atomic-number metals have been incorporated into luminescent molecules to enhance RTP intensity relative to fluorescence[2]. For example, heavy-atom-based RTP materials can improve the light-emitting diode device[16] efficiency in that triplet excitons may be the main (75%) excited-state species on electron–hole recombination[17]. The singlet–triplet energy gap, $|E_1 - E_3|$, on the other hand, may be controlled by boron dye loading, or in the case of dye-polymer conjugates, polymer-chain molecular weight. We have shown that fluorescence emission for BF_2dbmPLA powders varies over a 64 nm range depending on BF_2dbmPLA molecular weight (3–20 kDa, 507–443 nm respectively)[3]. High-molecular-weight samples exhibit blueshifted emission similar to solution, whereas increased fluorophore–fluorophore interactions in low-molecular-weight materials correspond to lower-energy, redshifted fluorescence.

Phosphorescence, in contrast, showed little change in energy or relative intensity with BF_2dbmPLA molecular weight, suggesting

---

[1]Department of Chemistry, University of Virginia, Charlottesville, Virginia 22904, USA, [2]Department of Radiation Oncology, Duke University Medical Center, Durham, North Carolina 27710, USA. *e-mail: fraser@virginia.edu.

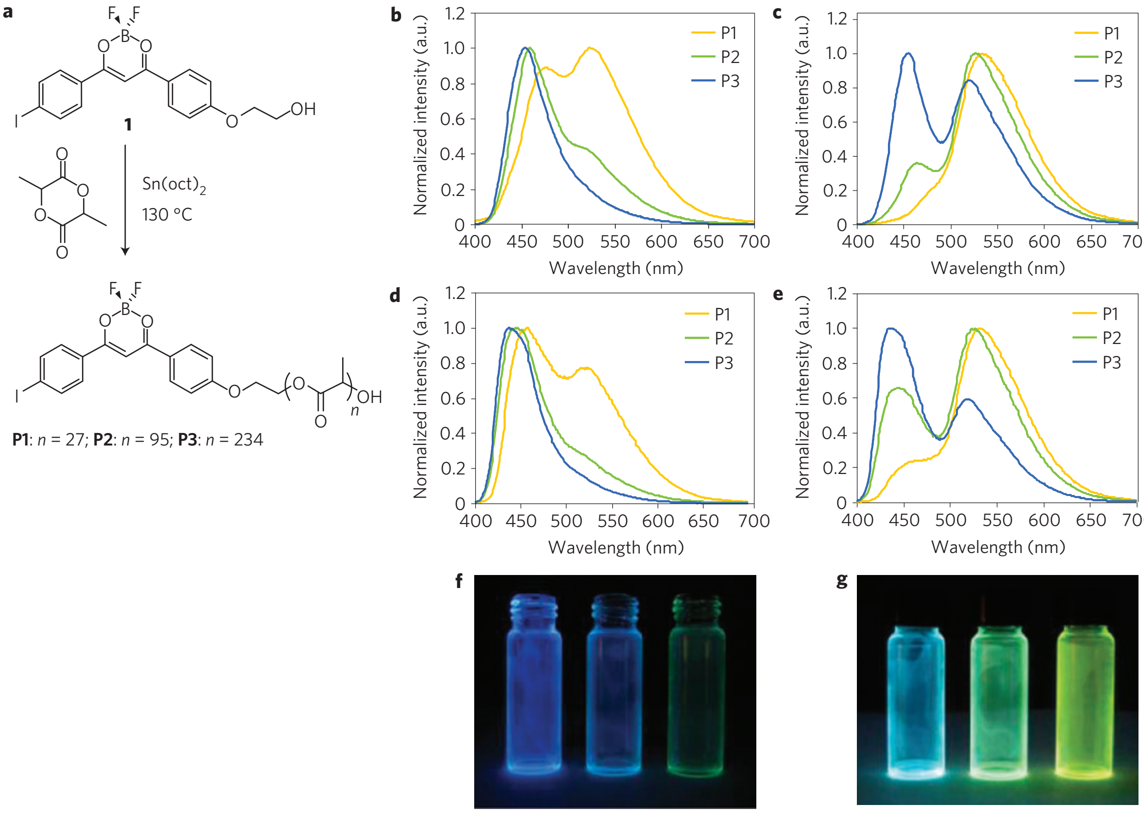

Figure 1 | Synthesis and solid-state emission of BF_2dbm(I)PLA (P1–P3). **a**, Ring-opening polymerization of BF_2dbm(I)PLA (**P1**–**P3**). **b**–**e**, Steady-state emission spectra of polymers **P1**–**P3** as powders (**b**,**c**) and spin-cast films (**d**,**e**) under air (**b**,**d**) and under N_2 (**c**,**e**). **f**,**g**, Simple-cast **P1**–**P3** (right to left) films in vials under air (**f**) and N_2 (**g**) (ultraviolet excitation: $\lambda_{ex} = 365$ nm).

Table 1 | Characterization of polymers P1–P3 in solution.

	M_n (Da)[*]	PDI[†]	λ_{abs} (nm)[‡]	ε (M^{-1} cm^{-1})[‡]	λ_F (nm)[§]	Φ_F[¶]	τ_F (ns)[‖]
1	458	1	407	58,000	441	0.55	1.03
P1	2,700	1.11	406	33,000	435	0.41	0.95
P2	7,300	1.15	406	40,000	436	0.44	0.96
P3	17,600	1.17	406	40,700	435	0.43	0.95

[*] In tetrahydrofuran versus polystyrene standards.

[†] Polydispersity index (PDI) = M_w/M_n.

[‡] ε: molar extinction coefficient. In CH_2Cl_2.

[§] Steady-state fluorescence spectra excited at 369 nm.

[¶] Fluorescence quantum yields in CH_2Cl_2 relative to anthracene in ethanol.

[‖] In CH_2Cl_2; excitation source: 369 nm light-emitting diode; fluorescence lifetime fit to single-exponential decay.

Table 2 | Luminescence characterization of P1–P3 in the solid state at 24 °C under nitrogen.

	Powder				Film			
	λ_F[*] (nm)	τ_F[†] (ns)	λ_{RTP}[‡] (nm)	τ_{RTP}[§] (ms)	λ_F[*] (nm)	τ_F[†] (ns)	λ_{RTP}[‡] (nm)	τ_{RTP}[§] (ms)
P1	485	0.37	535	4.06	458	0.48	532	4.25
P2	470	0.42	527	4.39	445	0.54	526	4.37
P3	456	0.43	525	4.50	438	0.64	523	4.41

[*] Steady-state fluorescence spectra excited at 369 nm.

[†] Excitation source: 369 nm light-emitting diode; fluorescence lifetime fit to triple-exponential decay.

[‡] Excitation source: xenon flash lamp at 405 nm.

[§] Excitation source: xenon flash lamp at 405 nm; RTP lifetime fit to triple-exponential decay.

that heavy-atom substitution may be necessary to augment the molecular-weight effect. On the basis of these arguments and previous observations, phosphorescence intensity is expected to be strongest for internal heavy-atom-modified materials with low molecular weights.

To test this idea, BF_2dbm(I)PLA samples with different molecular weights (**P1** = 2,700 Da, **P2** = 7,300 Da and **P3** = 17,600 Da) were prepared from a BF_2dbm(I)OH initiator, **1**, and lactide by solvent-free, tin-catalysed, controlled ring-opening polymerization (Fig. 1a, Supplementary Table S1). Polymers with low polydispersity indices (PDIs < 1.2) were obtained. The optical properties of **P1**–**P3** were first investigated in CH_2Cl_2 under air (Table 1). Under these conditions, all three polymers have nearly identical absorption ($\lambda_{abs} = 406$ nm) and emission spectra ($\lambda_F \sim 435$ nm, $\Phi_F \sim 0.4$, $\tau_F \sim 0.95$ ns) (see Supplementary Figs S1 and S2). As expected, iodide substitution results in enhanced intersystem crossing, lower Φ_F and shorter τ_F compared with hydrogen-substituted BF_2dbmPLA (ref. 6). Phosphorescence is absent for **P1**–**P3** in solution; RTP is a solid-state effect for these boron biomaterials.

For BF_2dbm(I)PLA powders, RTP and molecular-weight-dependent fluorescence emission colour tuning are expected and indeed observed. Correspondingly, two distinct emission bands were observed in spectra for **P2** (470 nm, 527 nm) and **P3** (456 nm, 525 nm), whereas, for low-molecular-weight **P1**, a single emission peak at 535 nm was evident with only a small shoulder at ~480 nm (Fig. 1c, Table 2). The higher energy band is attributed to fluorescence and the other much stronger, redshifted band is RTP emission. Under nitrogen, the emission colours of **P1**–**P3**

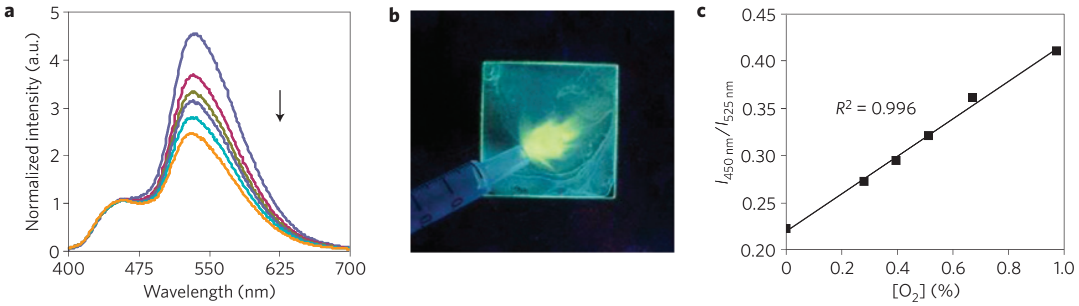

Figure 2 | Oxygen sensitivity for P1 BF_2dbm(I)PLA film. a, Emission spectra of the spin-cast film (**P1**) under increasing oxygen levels (indicated by the arrow, 0–1%) normalized to the fluorescence band. **b**, Image showing yellow phosphorescence emission under a N_2 gas stream for a spin-cast **P1** film under ultraviolet excitation. (Yellow phosphorescence turns on immediately on gas contact. Blue green background: weak **P1** fluorescence.) **c**, Linear relationship between oxygen level and the fluorescence/phosphorescence intensity ratio at two fixed wavelengths (450 nm and 525 nm).

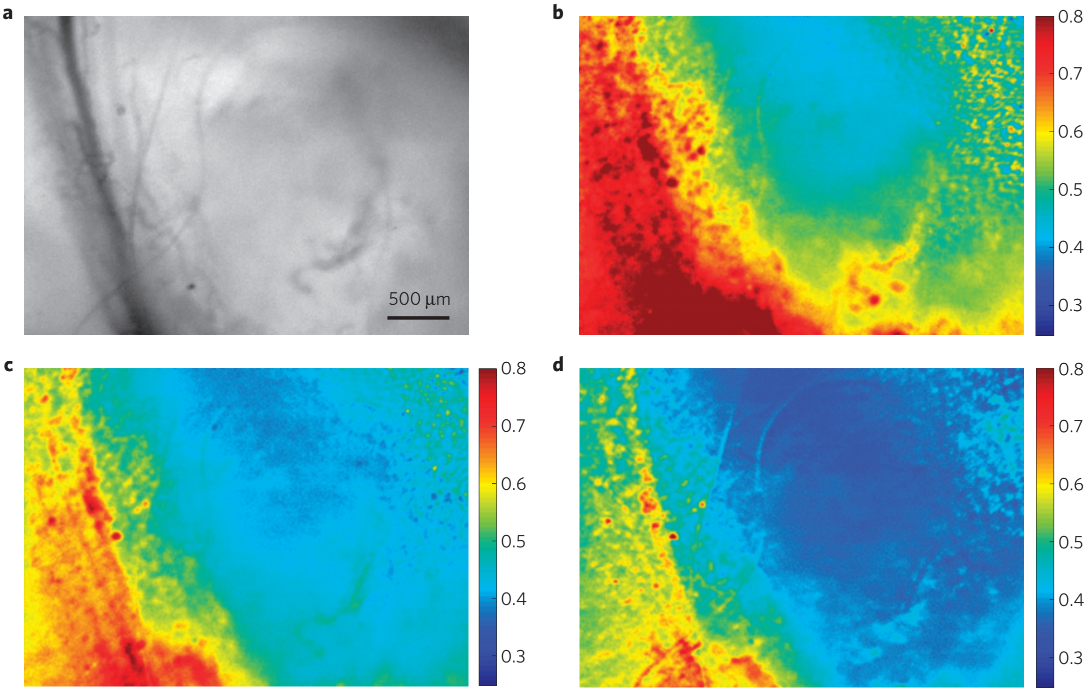

Figure 3 | Tumour hypoxia imaging with P2 BF_2dbm(I)PLA nanoparticles. a–c, *In vivo* imaging of the breast cancer 4 T1 mammary carcinoma tumour region in a mouse window chamber model showing the bright-field (**a**) and BNP fluorescence/phosphorescence ratio while breathing carbogen—95% O_2 (**b**), room air—21% O_2 (**c**) and nitrogen—0% O_2 (**d**). Emission intensity was averaged from 430 to 480 nm (fluorescence) and 530 to 600 nm (phosphorescence). Several blood vessels run vertically on the left side of the images (dark lines in the bright-field image; more oxygenated yellow–red regions in the fluorescence/phosphorescence images), with the tumour comprising the region to the right of the vessels (less-oxygenated blue regions in the fluorescence/phosphorescence images).

are greenish yellow, green and cyan respectively (Fig. 1g). Just as equation (1) predicts, as the energy gap, ΔE, decreases (that is, BF_2dbm(I)PLA molecular weight decreases), the singlet–triplet coupling becomes stronger (that is, larger δ), intersystem crossing is favoured and RTP intensity increases.

Luminescence lifetime data were also collected for **P1–P3** as powders (Table 2). All lifetimes fit to triple-exponential decay owing to the heterogeneity of the polymer matrix and possibly fluorophore–fluorophore interactions too. The fluorescence lifetimes become shorter (0.43–0.37 ns) as the polymer chain decreases (17.6–2.7 kDa) presumably owing to enhanced intersystem crossing (Table 1). Shorter RTP and delayed fluorescence lifetimes (**P1–P3**: 4.50–4.06 ms) with decreasing molecular weight suggest smaller singlet–triplet energy splitting where the thermal repopulation from triplet to singlet states is more probable[3]. Surprisingly, when the samples were exposed to air, long-lived RTP was still detectable (0.42, 0.55, 0.57 ms for **P1–P3**, respectively; see Supplementary Table S2). Consistent with the spectral data in Fig. 1b where RTP bands remain visible, these results indicate a much faster triplet decay rate compared with BF_2dbmPLA, which is entirely quenched in air. This suggests that radiative decay occurs on a comparable timescale to dynamic quenching, which is probably influenced by O_2 diffusion rates in the material[18].

Although the model predicts the observed fluorescence/phosphorescence control through heavy-atom assistance and polymer molecular weight, the experimental results exceeded our expectations. We discovered a tunability range that is nearly ideal, in terms of control and flexibility in oxygen sensor design. All **P1–P3** materials, regardless of molecular weight can be useful in lifetime or time-gated intensity-based sensing platforms. Those with comparable and readily detectable fluorescence and phosphorescence intensities (for example, **P2**) are beneficial for ratiometric hypoxia imaging, whereas, low-molecular-weight materials with weak to negligible fluorescence and strong phosphorescence (**P1**) serve as 'turn on' sensors that light up in anaerobic or low-oxygen environments. A simple demonstration of these effects is presented in Fig. 1, which shows changes in colour and brightness for **P1**–**P3** films under air (Fig. 1f) versus nitrogen (Fig. 1g). Thus, with a very simple molecular-weight adjustment, these boron biomaterials are easily tailored for different sensor platforms and imaging and detection schemes.

To explore oxygen sensitivity and processing effects in more detail and to demonstrate the relevance and versatility of this materials design concept for practical applications, boron biomaterials were fabricated as thin films and nanoparticles. Polymers **P1**–**P3** were cast from CH_2Cl_2 solutions ($5\,mg\,ml^{-1}$, or 0.3% w/w) onto glass substrates, followed by annealing at $\sim$110 °C for 10 s to improve film clarity. Under nitrogen, all three films showed visibly blueshifted colours compared with the powders. The steady-state emission spectra under air and nitrogen are given in Fig. 1d and e respectively, where it is noted that the fluorescence contributions are clearly larger than for the bulk polymer samples. Film fluorescence lifetimes are longer than their powder counterparts, suggesting decreased intersystem crossing perhaps due to diminished fluorophore–fluorophore interactions.

As a starting point for ratiometric oxygen sensing, the steady-state emission spectra of the **P1** film were recorded under different O_2 concentrations (Fig. 2a). The ratio of the invariant fluorescence ($\lambda_F = 458$ nm) to the oxygen-dependent RTP ($\lambda_P = 532$ nm) steadily increases with increasing oxygen levels (Fig. 2c). Up to 1% O_2, a linear dependency is observed ($R^2 = 0.996$). Beyond this point, the fluorescence/phosphorescence plot continues to rise up to ambient levels (that is, 21% O_2) but with curvature (Supplementary Fig. S3), possibly due to complicated dynamics in the heterogeneous polymer environment as previously reported[6]. Figure 2b shows the oxygen distribution on the surface of a **P1** film under ultraviolet excitation ($\lambda_{ex} = 365$ nm), where the bright yellow streaks provide clear visualization of nitrogen gas flow dynamics.

The polymer **P2**, with balanced fluorescence and phosphorescence emission, was also fabricated as boron nanoparticles (BNPs; 98 nm diameter) by nanoprecipitation[14]. The emission spectra ($\lambda_F = 450$ nm, $\lambda_{RTP} = 528$ nm; Supplementary Fig. S4), lifetimes ($\tau_F \sim 0.45$ ns, $\tau_{RTP} \sim 4.82$ ms) and oxygen calibration (Supplementary Fig. S5) are comparable to **P2** films. Fortuitously, the optimal linear range for this nanosensor ($\sim$0–3%) is in excellent correspondence with hypoxia in biological contexts. For example, tumour hypoxia ($pO_2 < 1\%$; ref. 19) is associated with increased invasiveness and resistance to radiation and chemotherapy. Despite its importance for cancer treatment and tumour biology[20], hypoxia is difficult to image with good spatial and temporal resolution, particularly in combination[21]. Given their small size, biocompatibility, photostability, dual-emissive features and high oxygen sensitivity, BNPs have the potential to address some of these challenges. To test their ability as ratiometric tumour hypoxia imaging agents, **P2** nanoparticles were used in combination with a mouse dorsal window chamber breast cancer 4T1 mammary carcinoma model for hyperspectral imaging[22]. Tissue oxygen maps of the window region presented as fluorescence/phosphorescence ratios during carbogen, air and brief nitrogen breathing (95, 21 and 0% O_2 respectively), show excellent contrast between the microvasculature (red) and the tumour tissue (blue), which remained hypoxic regardless of the breathing gas (Fig. 3). The signal was relatively stable $\sim$1–2 min after changing the breathing gas, which may be a function of the biology of tissue oxygen delivery and consumption more so than the inherent response of the nanosensors. The BNP tumour oxygenation maps are complementary to existing optical methods such as haemoglobin saturation imaging, which provides vascular oxygenation[22].

We have devised a simple yet powerful strategy for systematically tuning relative fluorescence and RTP intensities in a dual-emissive boron biomaterial. The experimental results support the proposed design concept involving manipulation of both spin–orbit coupling and singlet–triplet energy splitting. The wide-range fluorescence/phosphorescence tunability of boron biomaterials enables application in lifetime, time-gated intensity, ratiometric or 'turn on' sensing modes, and shows great promise for optical imaging, oxygen sensing and aerodynamics applications[4]. A new method for quantifying tumour hypoxia has also been demonstrated, and can further understanding of the relationship between hypoxia, tumour progression, metastasis and treatment resistance. This first demonstration of hypoxia imaging bodes well for using boron biomaterials for oxygen sensing in other biomedical and biotechnological contexts.

Methods

Molecular weights were determined by gel permeation chromatography (tetrahydrofuran, 20 °C, $1.0\,ml\,min^{-1}$) versus polystyrene standards on a Hewlett-Packard instrument (series 1100 HPLC) equipped with Polymer Laboratories 5 μm mixed-C columns and connected to ultraviolet–visible and refractive index (Viscotek LR 40) detectors. A 0.58 correction factor was applied[23,24]. Data were processed with the OmniSEC software (version 4.2, Viscotek Corp). Ultraviolet–visible spectra were recorded on a Hewlett-Packard 8453 diode array spectrophotometer. Photographs were taken in the dark using a Canon PowerShot SD600 Digital Elph camera with the automatic setting (no flash).

Powders were analysed as precipitated. A Laurell Technologies WS-650S spin-coater was used to cast polymer films for luminescence measurements with the default set-up (30 s at a constant speed of 4,000 r.p.m.). Boron polymer films were spin-cast from CH_2Cl_2 solutions ($\sim$2.5% w/w) onto Fischer Scientific glass cover slides (22 × 22 mm) at a spin speed of 4,000 r.p.m. The coated slides were cut into $\sim$3 mm × 22 mm strips, placed in a transparent glass vial under a N_2 atmosphere and were sealed with Teflon caps for measurements. (Note: both borosilicate glass cover slides and glass vials are optically inactive using an excitation wavelength of greater than 368 nm.)

Steady-state fluorescence emission spectra were recorded on a Horiba Fluorolog-3 Model FL3-22 spectrofluorometer (double-grating excitation and double-grating emission monochromators). For all luminescence measurements, a Tiffen 55 mm 0.9 neutral density filter was placed in the path of the excitation source to protect the sample from photobleaching. RTP spectra were recorded with the same instrument except that a pulsed xenon lamp ($\lambda_{ex} = 369$ nm; duration < 1 ms) was used and spectra were collected with a 1 ms delay after excitation. Time-correlated single-photon counting fluorescence lifetime measurements were carried out with a NanoLED-370 (369 nm) excitation source and a DataStation Hub as the single-photon counting controller. Phosphorescence lifetimes were measured with a 500 ns multi channel scalar card excited with a pulsed xenon lamp ($\lambda_{ex} = 369$ nm; duration < 1 ms). Lifetime data were analysed with DataStation v2.4 software from Horiba Jobin Yvon.

Fluorescence quantum yields, Φ_F, for BF_2dbm(I)OH (**1**) and BF_2dbm(I)PLA (**P1**–**P3**) in CH_2Cl_2 were calculated versus anthracene in ethanol as a standard, as previously described[25] using the following values: Φ_F anthracene = 0.27 (ref. 26), n_D^{20} ethanol = 1.360, n_D^{20} CH_2Cl_2 = 1.424; n_D^{20} is the refractive index (20 °C, yellow sodium D line, 589 nm). Optically dilute CH_2Cl_2 solutions of BF_2dbm(I)OH and BF_2dbm(I)PLA, and ethanol solutions of the anthracene standard were prepared in 1-cm-path-length quartz cuvettes, and absorbances ($A < 0.1$) were recorded and steady-state emission spectra were obtained ($\lambda_{ex} = 350$ nm; emission integration range: 365–700 nm).

For oxygen sensitivity and intensity-based Stern–Volmer plot measurements, gas mixtures of O_2 and N_2 of various concentrations were prepared by using two Cole-Parmer 65 mm flow meters. For each concentration, the pre-mixed gas was passed through a 1-m-path quartz fluorometer cell equipped with a septum screw top containing the spin-cast **P1** film for 15 min and then the spectrum was recorded. The oxygen sensitivity for the **P2** nanoparticle aqueous suspension was calibrated similarly except that the pre-mixed gas was first evenly dispensed into a distilled-water chamber before passing through a quartz cell containing 1 ml of the optically dilute (abs < 0.1) sample.

A window chamber was implanted using previously described techniques[22]. Briefly, the mouse was anaesthetized using an intraperitoneal injection of $100\,mg\,kg^{-1}$ ketamine, $10\,mg\,kg^{-1}$ xylazine. The skin on the back of the animal was stretched into a metal frame to enable insertion of a titanium window frame, having a 12-mm-diameter window. The front face of the skin fold was excised, and approximately 20,000 4T1 murine mammary carcinoma cells were injected into the underlying fascia. A cover glass was placed over the open face of the window, and the tumour was allowed to incubate for 10 days before imaging.

An approximately 100 μl suspension of **P2** nanoparticles ($\sim 1\,mg\,ml^{-1}$) was injected into the space between the window chamber and the cover glass.

Approximately 5 min passed between the injection and imaging, which allowed for stabilization of the signal. The animal was placed on an upright fluorescence microscope equipped with a DAPI excitation filter, and a liquid-crystal tunable emission filter (VariSpec, Cambridge Research and Instrumentation). This enabled acquisition of an emission spectrum, which was acquired in 10 nm intervals from 430 to 600 nm. Gas was administered by a nose cone at a rate of 5 l min^{-1}, except for room air, during which the gas was shut off. The carbogen breathing was begun at the beginning of the experiment, with approximately 5 min passing before the initial acquisition. The gas was then switched to room air for a period of 3 min, and finally nitrogen for 30 s. The images shown in Fig. 3 were taken at the end of each respective period of gas breathing. Data were processed by taking the ratio of the fluorescence to phosphorescence signals, which were defined as the average signal acquired from 430 to 480 nm and 530 to 600 nm, respectively.

Received 19 March 2009; accepted 8 July 2009; published online 9 August 2009

References

1. Yuste, R. Fluorescence microscopy today. *Nature Methods* **2,** 902–904 (2005).
2. Lower, S. K. & El-Sayed, M. A. The triplet state and molecular electronic processes in organic molecules. *Chem. Rev.* **66,** 199–241 (1966).
3. Zhang, G., Kooi, S. E., Demas, J. N. & Fraser, C. L. Emission colour tuning with polymer molecular weight for boron dibenzoylmethane-polylactide. *Adv. Mater.* **20,** 2099–2104 (2008).
4. Köse, M. E., Omar, A., Virgin, C. A., Carroll, B. F. & Schanze, K. S. Principal component analysis calibration method for dual-luminophore oxygen and temperature sensor films: Application to luminescence imaging. *Langmuir* **21,** 9110–9120 (2005).
5. Koo, Y. E. L. *et al.* Real-time measurements of dissolved oxygen inside live cells by organically modified silicate fluorescent nanosensors. *Anal. Chem.* **76,** 2498–2505 (2004).
6. Zhang, G. *et al.* Multi-emissive difluoroboron dibenzoylmethane polylactide exhibiting intense fluorescence and oxygen sensitive room temperature phosphorescence. *J. Am. Chem. Soc.* **129,** 8942–8943 (2007).
7. Scypinski, S. & Love, L. J. C. Room-temperature phosphorescence of polynuclear aromatic hydrocarbons in cyclodextrins. *Anal. Chem.* **56,** 322–327 (1984).
8. Mitchell, C. A., Gurney, R. W., Jang, S.-H. & Kahr, B. On the mechanism of matrix-assisted room temperature phosphorescence. *J. Am. Chem. Soc.* **120,** 9726–9727 (1998).
9. Carretero, A. S., Castillo, A. S. & Gutiérrez, A. F. A review of heavy-atom-induced room-temperature phosphorescence: A straightforward phosphorimetric method. *Crit. Rev. Anal. Chem.* **35,** 3–14 (2005).
10. Chow, Y. L., Cheng, X. C. & Johansson, C. I. Molecular interactions of dibenzoylmethanatoboron difluoride (DBMBF$_2$) in the excited and ground states in solution. *J. Photochem. Photobiol. A* **57,** 247–255 (1991).
11. Cogné-Laage, E. *et al.* Diaroyl(methanato)boron difluoride compounds as medium sensitive two-photon fluorescent probes. *Chem. Eur. J.* **10,** 1445–1455 (2004).
12. Nagai, A., Kokado, K., Nagata, Y. & Chujo, Y. 1,3-Diketone-based organoboron polymers: Emission by extending π-conjugation along a polymeric ligand. *Macromolecules* **41,** 8295–8298 (2008).
13. Qin, Y., Kiburu, I., Shah, S. & Jäkle, F. Synthesis and characterization of organoboron quinolate polymers with tunable luminescence properties. *Macromolecules* **39,** 9041–9048 (2006).
14. Pfister, A., Zhang, G., Zareno, J., Horwitz, A. F. & Fraser, C. L. Boron polylactide nanoparticles exhibiting fluorescence and phosphorescence in aqueous medium. *ACS Nano* **2,** 1252–1258 (2008).
15. McClure, D. S. Triplet–singlet transitions in organic molecules. Lifetime measurements of the triplet state. *J. Chem. Phys.* **17,** 905–913 (1949).
16. Adachi, C., Baldo, M. A., Thompson, M. E. & Forrest, S. R. Nearly 100% internal phosphorescence efficiency in an organic light-emitting device. *J. Appl. Phys.* **90,** 5048–5051 (2001).
17. Baldo, M. A., O'Brien, D. F., Thompson, M. E. & Forrest, S. R. Excitonic singlet–triplet ratio in a semiconducting organic thin film. *Phys. Rev. B* **60,** 14422–14428 (1999).
18. Twarowski, A. J. & Good, L. Phosphorescence quenching by molecular oxygen: Zinc tetraphenylporphin on solid supports. *J. Phys. Chem.* **91,** 5252–5257 (1987).
19. Höckel, M. & Vaupel, P. Tumor hypoxia: Definitions and current clinical, biologic, and molecular aspects. *J. Natl Cancer Inst.* **93,** 266–276 (2001).
20. Harris, A. L. Hypoxia—a key regulatory factor in tumour growth. *Nature Rev. Cancer* **2,** 38–47 (2002).
21. Dewhirst, M. W. *et al.* Review of methods used to study oxygen transport at the microcirculatory level. *Int. J. Cancer* **90,** 237–255 (2000).
22. Sorg, B. S., Moeller, B. J., Donovan, O., Cao, Y. & Dewhirst, M. W. Hyperspectral imaging of hemoglobin saturation in tumor microvasculature and tumor hypoxia development. *J. Biomed. Opt.* **10,** 44004 (2005).
23. Baran, J., Duda, A., Kowalski, A., Szymanski, R. & Penczek, S. Intermolecular chain transfer to polymer with chain scission: General treatment and determination of k_p/k_{tr} in L, L-lactide polymerization. *Macromol. Rapid Commun.* **18,** 325–333 (1997).
24. Save, M., Schappacher, M. & Soum, A. Controlled ring-opening polymerization of lactones and lactides initiated by lanthanum isopropoxide, 1. General aspects and kinetics. *Macromol. Chem. Phys.* **203,** 889–899 (2002).
25. Crosby, G. A. & Demas, J. N. Measurement of photoluminescence quantum yields. *J. Phys. Chem.* **75,** 991–1024 (1971).
26. Melhuish, W. H. Quantum efficiencies of fluorescence of organic substances: Effect of solvent and concentration of the fluorescent solute. *J. Phys. Chem.* **65,** 229–235 (1961).

Acknowledgements

We thank the National Science Foundation (C.L.F.: CHE 0718879), the Department of Defense (G.M.P.: Postdoctoral Fellowship W81XWH-07-1-0355) and the NIH (M.W.D.: R01CA40355) for support for this research. We are also grateful to the UVA NanoSTAR Institute and the UVA Cancer Center through the James and Rebecca Craig Foundation and the NCI Cancer Center Support Grant P30 CA44579 for supporting our efforts to develop and test BNPs as biomedical imaging agents. We thank J. N. Demas for helpful discussions and R. E. Evans for assistance.

Author contributions

G.Z and C.L.F. are responsible for materials design, synthesis and characterization and manuscript preparation. G.M.P. and M.W.D. are responsible for tumour hypoxia imaging studies and data analysis.

Additional information

Supplementary information accompanies this paper on www.nature.com/naturematerials. Reprints and permissions information is available online at http://npg.nature.com/reprintsandpermissions. Correspondence and requests for materials should be addressed to C.L.F.

Combined hyperspectral and spectral domain optical coherence tomography microscope for noninvasive hemodynamic imaging

Melissa C. Skala,[1,*] **Andrew Fontanella,**[2] **Hansford Hendargo,**[1] **Mark W. Dewhirst,**[2] **and Joseph A. Izatt**[1]

[1]*Department of Biomedical Engineering, Duke University, Durham, North Carolina 27708, USA*
[2]*Department of Radiation Oncology, Duke University, Durham, North Carolina 27710, USA*
**Corresponding author: melissa.skala@duke.edu*

Received October 27, 2008; accepted November 27, 2008;
posted December 18, 2008 (Doc. ID 102438); published January 26, 2009

We have combined hyperspectral imaging with spectral domain optical coherence tomography (SDOCT) to noninvasively image changes in hemoglobin saturation, blood flow, microvessel morphology, and sheer rate on the vessel wall with tumor growth. Changes in these hemodynamic variables were measured over 24 h in dorsal skin fold window chamber tumors. There was a strong correlation between volumetric flow and hemoglobin saturation ($\rho=0.89$, $p=9\times10^{-6}$, $N=15$) and a moderate correlation between shear rate on the vessel wall and hemoglobin saturation ($\rho=0.56$, $p=0.03$, $N=15$). © 2009 Optical Society of America

OCIS codes: 170.4500, 110.4234, 170.2655, 170.3880.

Hypoxia is important in regulating tumor aggressiveness and treatment resistance and thus serves as a valuable biomarker for tumor treatment outcome. A better understanding of tumor microcirculation would provide a basis for improved prognostic and treatment approaches for solid tumors. In tumors, formation of new vessels and remodeling and dropout of existing vessels occurs continuously, resulting in temporal variations in flow and oxygenation [1]. Dynamic imaging of vessel morphology, hemoglobin oxygen saturation, blood flow, and shear rate on the vessel wall would provide valuable insight into the mechanisms and distribution of cycling hypoxia in growing tumors. For example, these data will allow for direct observation of tumor microvessel response to changing hemodynamic and metabolic conditions induced by cancer treatments.

Tumor hemodynamics on the microvascular level have traditionally been studied with invasive methods or highly localized (nonimaging) methods. Confocal or multiphoton microscopy coupled with a vascular contrast agent has been widely used in animal models to track changes in vessel morphology [2]. Blood flow in small vessels has been limited to point measurements using video-rate microscopy and single cell counting [1] or laser Doppler flowmetry [3]. Tumor oxygenation has been quantified with fluorescence lifetime imaging of a pO_2 calibrated dye [4] or with microelectrode measurements [3]. Point measurements of shear rates on vessel walls have also been estimated with video microscopy [5]. Noninvasive imaging methods are currently emerging to replace these traditional techniques. Speckle variance optical coherence tomography (OCT) has recently shown promise for monitoring changes in vessel morphology with photodynamic therapy in the dorsal skin fold window chamber [2]. Doppler OCT imaging of blood flow direction and velocity profiles within vessels [6], and hyperspectral imaging of tumor hemoglobin oxygenation saturation [7], have also been shown separately to provide valuable information on tumor vessel function. However, a complete picture of tumor hemodynamics requires multidimensional image data including vessel morphology, blood velocity profiles and direction of flow, and hemoglobin oxygen saturation.

We have combined hyperspectral imaging with OCT to noninvasively image changes in vascular morphology, hemoglobin oxygen saturation, blood velocity and direction of flow, and shear rate on the vessel wall with tumor growth. This combined microscope provides a wealth of information on the dynamics of structural and functional changes in tumor vasculature. Hyperspectral (hemoglobin oxygen saturation) and spectral domain OCT (SDOCT) (blood flow and vascular morphology) arms were connected through two separate baseports in an inverted microscope (Carl Zeiss Axiovert 200) (Fig. 1). Two-dimensional hyperspectral images were collected with a 100 W halogen lamp for transillumination, and detection was achieved with a liquid-crystal tunable filter (LCTF) (CRI, Inc.) placed in front of a DVC 1412 CCD camera (DVC Company) [7]. Custom software was used to tune the filter and acquire images at 10 nm increments between 500 and 610 nm. Measurements of the dark offset and transmission through a neutral density filter at each wavelength were made before each imaging session. Hemoglobin saturation images were calculated by applying an extension of the Beer–Lambert law to the wavelength-dependent absorption at each pixel (assuming oxygenated and deoxygenated hemoglobin as the only absorbers), and then solving for hemoglobin saturation with linear least-squares regression [7]. The sys-

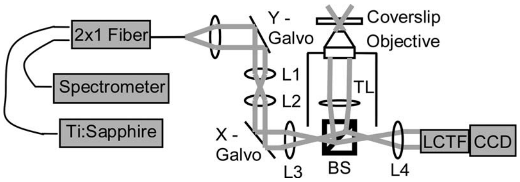

Fig. 1. Schematic of the combined hyperspectral–SDOCT microscope. L1–L4, lenses 1–4; TL, tube lens; BS, beam splitter; LCTF, liquid-crystal tunable filter.

0146-9592/09/030289-3/$15.00 © 2009 Optical Society of America

tem, software, and analysis techniques have previously been validated on liquid phantoms with an accuracy of approximately 1% and *in vivo* [7].

The common-path spectral domain OCT arm consists of a Ti:sapphire laser source (Femtolasers) centered at 790 nm with a 90 nm FWHM. The interferogram is detected using a custom-made spectrometer with a line-scan CCD camera (Atmel, Aviiva). The OCT system is driven by software that controls the lateral scanner and performs data acquisition and archiving (Bioptigen, Inc.). Three-dimensional blood flow images were collected with Doppler OCT, which measures phase changes due to flowing erythrocytes. Phase changes are calculated from multiple *A* scans collected at the same position in the volume, and can be related to flow velocity profiles by measuring the angle of incidence in the three-dimensional volume. Three-dimensional morphology was collected with speckle variance OCT, which detects blood vessels from the variance in the speckle pattern between sequential *B*-scan magnitude images [2]. Speckle variance is advantageous for morphology mapping, because it is independent of the angle between the blood flow and the incident beam. However, it is currently not capable of accurately quantifying blood velocity or flow direction.

Hyperspectral, Doppler OCT, and speckle variance OCT images were collected from 4T1 tumors implanted in dorsal skin fold window chambers in nude mice. Surgery and imaging were carried out under ketamine–xylazine and isoflurane anesthesia, respectively, with the mice maintained at body temperature (conducted with institutional approval at Duke University). The transmission image of the window chamber morphology (Fig. 2A) and hyperspectral image of the percent hemoglobin oxygenation saturation in the vessels (Fig. 2C) were taken with a 2.5× objective (NA=0.12). Speckle variance OCT (Fig. 2B) provides three-dimensional vessel morphology, and Doppler OCT (Fig. 2D) provides three-dimensional vessel flow velocities and flow direction. Speckle variance and Doppler OCT images were collected over a 1 mm × 1 mm area with 250 × 125 pixels, and 1024 pixels in the depth dimension. OCT images were collected with a 4× objective (NA =0.1) with a 1 ms integration time for each *A* line. Eight repeated *B* scans were collected for speckle variance OCT, registered using "stackreg" for ImageJ, and 10 repeated *A* scans were colleted for Doppler OCT. The flow profiles in Figs. 2E and 2F were fit to a second-order polynomial and corrected for the angle of incidence to provide velocity in millimeters per second. Maximum blood velocity is determined from the peak of this fit, vessel diameter is determined from the zero crossings of the fit, and the shear rate on the vessel wall is calculated from the derivative of the fit (dv_z/dr), assuming a Newtonian fluid [8]. Coregistration of speckle variance OCT, hyperspectral, and Doppler OCT images allow for vessel morphology, percent hemoglobin oxygen saturation, blood velocity and direction of flow, and shear rate on the vessel to be determined at any point within the window chamber.

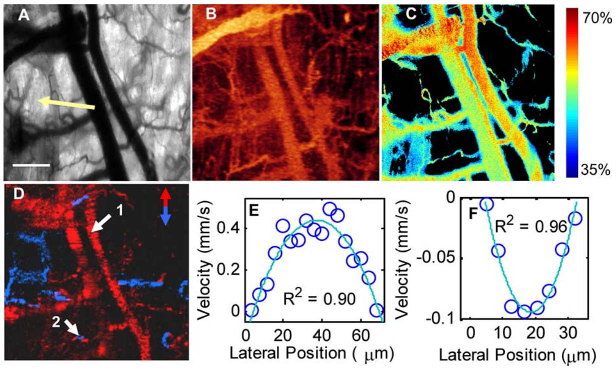

Fig. 2. (Color online) Multidimensional functional imaging of 4T1 tumor vasculature in the dorsal skin fold mouse window chamber. Transmission image of the window chamber taken with the liquid crystal tunable filter set at 500 nm, with a portion of the tumor visible (arrow, A). Scale bar is 200 μm. B, Speckle variance OCT image of vessel morphology shown as an *en face* average intensity projection over 1 mm depth. C, Hyperspectral image of percent hemoglobin oxygen saturation, thresholded for the *R*-squared value of the linear fit and total absorption value at each pixel (background pixels are black). D, Doppler OCT image of vessel blood flow direction shown as an *en face* maximum intensity projection over depth, with red vessels (1) flowing toward the top of the image and blue vessels (2) flowing toward the bottom of the image. The flow profiles at points 1 (E) and 2 (F) were fit to a second-order polynomial and corrected for the angle of incidence to provide velocity in millimeters per second.

Changes in hemoglobin saturation, vessel morphology, and blood flow with tumor growth were measured in a 14-day-old 4T1 tumor in the dorsal skin fold window chamber (Fig. 3). Hyperspectral and Doppler OCT data sets were collected every 6 h for 24 h. The blood velocity and hemoglobin saturation as a function of time are shown for three vessel cross sections of interest (VOIs) in Fig. 3. The measured hemoglobin saturation values fall within the expected range [9,10]. Note that the pO_2 of peripheral arteries in both tumors [9] and normal tissues [10]

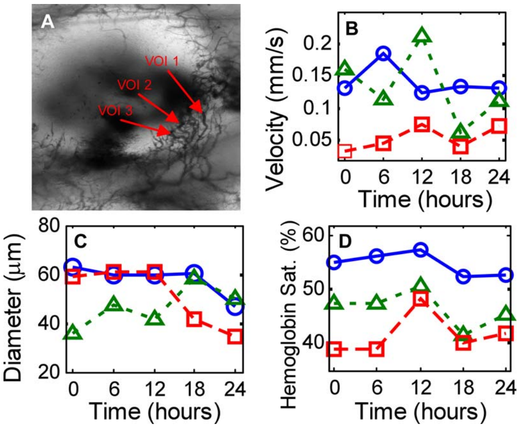

Fig. 3. (Color online) Time series data taken from a 4T1 window chamber tumor using the combined hyperspectral–OCT microscope. The transmission image (A) is 3 mm (height) × 2 mm (width) and delineates the three VOIs for which maximum blood velocity (B), diameter (C), and hemoglobin saturation (D) are plotted (open circles, VOI 1; open triangles, VOI 2; open squares, VOI 3).

can be substantially less than 95% saturated owing to loss of oxygen from the peripheral arterial tree (longitudinal oxygen gradient). The extracted maximum velocities and vessel diameters are in agreement with previously published values from the window chamber model [11]. Variations in red blood cell flux and pO_2 [1], hemoglobin oxygen saturation [7], and diameter [9] have previously been observed in tumors over time scales ranging from one hour to several days.

The relationship between the maximum velocity, diameter, flow rate, shear rate, and hemoglobin oxygen saturation for the same three vessels is shown in Fig. 4. Spearman rank correlation analysis of the three vessels over five time points revealed a strong correlation ($\rho=0.94$, $p=0.018$, $N=5$) between vessel hemoglobin saturation and maximum vessel velocity for VOI 2 (Fig. 4B) and no significant correlation for VOI 1 or VOI 3 ($p>0.05$, Figs. 4A and 4C). There was no correlation between vessel diameter and maximum velocity or between vessel diameter and hemoglobin saturation for any of the VOIs ($p>0.05$). The flow rate $[Q=\pi^*(D/2)^2 * V_{\max}/2(\mathrm{mm}^3/\mathrm{s})]$ was calculated from the vessel diameter (D) and maximum vessel velocity ($V_{\max}$). For all three VOIs and five time points grouped together, there was a strong correlation between velocity and hemoglobin saturation (Fig. 4D, $\rho=0.78$, $p=0.0006$, $N=15$), and between flow rate and hemoglobin saturation (Fig. 4E, $\rho=0.89$, $p=9\times10^{-6}$, $N=15$), and a moderate correlation between shear rate on the vessel wall and hemoglobin saturation (Fig. 4F, $\rho=0.56$, $p=0.03$, $N=15$). Shear rate values are in qualitative agreement with previous studies employing different techniques [5].

Previous studies [1,4] indicate that vessel remodeling with tumor growth alters flow distributions, and the relationship between hemoglobin oxygen saturation and blood flow in tumors is heterogeneous. However, the techniques employed in previous studies have a significant effect on the results. The dual slit technique suffers from inaccurate estimations of the length traveled by red blood cells, because the length of a three-dimensional vessel is projected onto a two-dimensional image, resulting in imprecise velocity values. Red blood cell flux measurements are limited to vessels smaller than ~30 μm in diameter, because individual red blood cells are difficult to visualize in larger vessels. Also, previous studies measured intravascular and extravascular pO_2, rather than hemoglobin saturation. The techniques demonstrated in the current study are advantageous, because flow velocity profiles can be accurately measured from a wide range of vessel diameters, and morphology, blood oxygen saturation, and blood velocity can be accurately determined without the use of contrast agents.

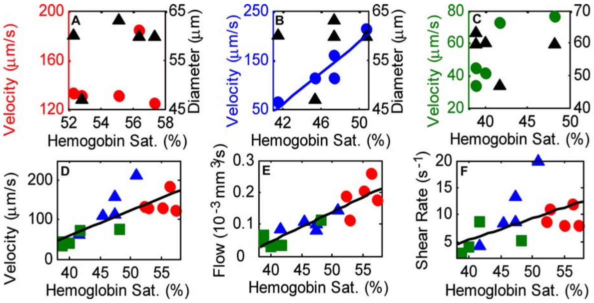

Fig. 4. (Color online) Scatter plots of maximum velocity vs. hemoglobin saturation (○) and diameter vs. hemoglobin saturation (▲) for VOI 1 (A), VOI 2 (B), and VOI 3 (C). There was a strong correlation (B) between the maximum velocity and hemoglobin saturation for VOI 2 ($\rho=0.94$, $p=0.018$, $N=5$), and no correlation for any other VOI ($p>0.05$). However, when all VOI (○, VOI 1; ▲, VOI 2; □, VOI 3) and time points were grouped together (D), there was a strong correlation between maximum velocity and hemoglobin saturation ($\rho=0.78$, $p=0.0006$, $N=15$). There was also a strong correlation (E) between flow (vessel cross sectional area times $\frac{1}{2}$ maximum velocity) and hemoglobin saturation ($\rho=0.89$, $p=9\times10^{-6}$, $N=15$) and a moderate correlation (F) between shear rate on the vessel wall and hemoglobin saturation ($\rho=0.56$, $p=0.03$, $N=15$) when all VOI and time points were grouped together.

We have combined hyperspectral microscopy with OCT to create a tool that can dynamically and noninvasively monitor vessel structure and function. These combined measurements will allow for unprecedented insight into the relationship among vessel structure, hemoglobin saturation, blood flow, and hypoxic episodes in tumors. This research instrument could ultimately lead to a more detailed understanding of the structural and functional properties of tumor vasculature and potentially become a valuable tool for screening tumor therapies in animal models.

This research was supported by the National Institutes of Health (NIH)–National Cancer Institute (NCI) grant CA40355 and NIH grant R21 EB006338. M. C. Skala acknowledges fellowship support through the NIH–NCI (F32 CA130309).

References

1. J. Lanzen, R. D. Braun, B. Klitzman, D. Brizel, T. W. Secomb, and M. W. Dewhirst, Cancer Res. **66**, 4 (2006).
2. A. Mariampillai, B. A. Standish, E. H. Moriyama, M. Khurana, N. R. Munce, M. K. Leung, J. Jiang, A. Cable, B. C. Wilson, I. A. Vitkin, and V. X. Yang, Opt. Lett. **33**, 13 (2008).
3. R. D. Braun, J. L. Lanzen, and M. W. Dewhirst, Am. J. Physiol. **277**, 2 (1999).
4. G. Helmlinger, F. Yuan, M. Dellian, and R. K. Jain, Nat. Med. **3**, 2 (1997).
5. Y. Tsuzuki, D. Fukumura, B. Oosthuyse, C. Koike, P. Carmeliet, and R. K. Jain, Cancer Res. **60**, 22 (2000).
6. V. X. Yang, S. J. Tang, M. L. Gordon, B. Qi, G. Gardiner, M. Cirocco, P. Kortan, G. B. Haber, G. Kandel, I. A. Vitkin, B. C. Wilson, and N. E. Marcon, Gastrointest. Endosc. **61**, 7 (2005).
7. B. S. Sorg, B. J. Moeller, O. Donovan, Y. Cao, and M. W. Dewhirst, J. Biomed. Opt. **10**, 4 (2005).
8. T. G. van Leeuwen, M. D. Kulkarni, S. Yazdanfar, A. M. Rollins, and J. A. Izatt, Opt. Lett. **24**, 22 (1999).
9. M. W. Dewhirst, E. T. Ong, G. L. Rosner, S. W. Rehmus, S. Shan, R. D. Braun, D. M. Brizel, and T. W. Secomb, Br. J. Cancer Suppl. **27**, S241 (1996).
10. B. R. Duling and R. M. Berne, Circ. Res. **27**, 5 (1970).
11. M. W. Dewhirst, R. Oliver, C. Y. Tso, C. Gustafson, T. Secomb, and J. F. Gross, Int. J. Radiat. Oncol. Biol. Phys. **18**, 3 (1990).

Journal of Biomedical Optics 15(1), 011112 (January/February 2010)

Longitudinal optical imaging of tumor metabolism and hemodynamics

Melissa C. Skala
Andrew Fontanella
Duke University
Department of Biomedical Engineering
136 Hudson Hall, Box 90281
Durham, North Carolina 27708

Lan Lan
Duke University
Department of Biostatistics and Bioinformatics
Box 2721
Durham, North Carolina 27710

Joseph A. Izatt
Duke University
Department of Biomedical Engineering
136 Hudson Hall, Box 90281
Durham, North Carolina 27708

Mark W. Dewhirst
Duke University
Department of Radiation Oncology
Box 3455
Durham, North Carolina 27710

Abstract. An important feature of tumor hypoxia is its temporal instability, or "cycling hypoxia." The primary consequence of cycling hypoxia is increased tumor aggressiveness and treatment resistance beyond that of chronic hypoxia. Longitudinal imaging of tumor metabolic demand, hemoglobin oxygen saturation, and blood flow would provide valuable insight into the mechanisms and distribution of cycling hypoxia in tumors. Fluorescence imaging of metabolic demand via the optical redox ratio (fluorescence intensity of FAD/NADH), absorption microscopy of hemoglobin oxygen saturation, and Doppler optical coherence tomography of vessel morphology and blood flow are combined to noninvasively monitor changes in oxygen supply and demand in the mouse dorsal skin fold window chamber tumor model (human squamous cell carcinoma) every 6 h for 36 h. Biomarkers for metabolic demand, blood oxygenation, and blood flow are all found to significantly change with time ($p < 0.05$). These variations in oxygen supply and demand are superimposed on a significant ($p < 0.05$) decline in metabolic demand with distance from the nearest vessel in tumors (this gradient was not observed in normal tissues). Significant ($p < 0.05$), but weak ($r \leq 0.5$) correlations are found between the hemoglobin oxygen saturation, blood flow, and redox ratio. These results indicate that cycling hypoxia depends on both oxygen supply and demand, and that noninvasive optical imaging could be a valuable tool to study therapeutic strategies to mitigate cycling hypoxia, thus increasing the effectiveness of radiation and chemotherapy. [DOI: 10.1117/1.3285584]

Keywords: tumor hypoxia; cycling; longitudinal imaging; tumor metabolism.

Paper 09287SSR received Jul. 7, 2009; revised manuscript received Oct. 26, 2009; accepted for publication Oct. 27, 2009; published online Jan. 13, 2010.

1 Introduction

Hypoxic tumors are more aggressive than their normoxic counterparts, and are resistant to radiation and chemotherapy.[1–3] Thus, a major goal of cancer research is to gain a better understanding of oxygen supply and demand in tumors. Studies of oxygen supply and demand could provide a basis for improved prognostic and treatment approaches for solid tumors. An important feature of tumor hypoxia is its temporal instability. "Cycling hypoxia" has been described as a pattern of temporal periodicity between hypoxic and reoxygenated states. It has been observed in many tumor types,[4–6] whereas studies measuring pO_2 fluctuations in normal tissue (muscle) in rats and mice have not observed significant fluctuations.[7,8] One primary consequence of cycling hypoxia is upregulation of the transcription factor hypoxia-inducible factor 1 (HIF1) activity to a level that supersedes that of chronic hypoxia. This transcription factor controls many cellular functions that exacerbate treatment resistance and tumor aggressiveness.[9]

Cycling hypoxia could be caused by changes in tumor vascular function (oxygen delivery) and metabolic demand. In tumors, formation of new vessels and remodeling and dropout of existing vessels occurs continuously, resulting in temporal variations in blood flow and blood oxygenation.[10] Oxygen consumption rate is a highly dynamic feature of oxygen transport in tumors, because small changes in demand for oxygen create large changes in the extent and severity of hypoxia.[11] Longitudinal imaging of tumor metabolic demand, vessel morphology, hemoglobin oxygen saturation, and blood flow velocities would provide valuable insight into the mechanisms and distribution of cycling hypoxia in tumors. For example, these data will allow for the study of tumor response to changing hemodynamic and metabolic conditions induced by experimental and traditional cancer therapies. Such information can also be used to test and refine theoretical models for structural adaptation in tumors, which have successfully predicted tumor response to drug and radiation therapy.[12]

Address all correspondence to Melissa C. Skala, Duke University, Department of Biomedical Engineering, 136 Hudson Hall, Box 90281, Durham, North Carolina 27708. Tel: 919-660-5588; Fax: 919-684-4488; E-mail: melissa.skala@duke.edu

1083-3668/2010/15(1)/011112/8/$25.00 © 2010 SPIE

Current methods for measuring oxygen supply on the microvessel level include microelectrode measurements,[7] and phosphorescence lifetime imaging of a pO_2 calibrated dye.[13] Microelectrodes provide a sensitive and direct measure of pO_2, but are inherently invasive and limited to point measurements. Phosphorescence lifetime imaging provides information on the 2-D distribution of oxygen within the tumor, but requires the injection of a contrast agent. The use of a contrast agent is invasive and may require repeated exposure to the dye for longitudinal measurements, which further complicates data acquisition and interpretation. Blood flow on the microvessel level has traditionally been measured using laser Doppler flowmetry,[7] the dual-slit method,[13] or video microscopy.[14,15] Laser Doppler flowmetry provides a relative (not calibrated) measurement of blood flow at a single point, and scanning laser Doppler provides an average flow over a tissue area without accounting for contributions from individual vessels. The dual-slit technique and video microscopy both suffer from inaccurate estimations of the length traveled by red blood cells because the length of a 3-D vessel is projected onto a 2-D image, resulting in imprecise velocity values. Video microscopy of fluorescently labeled red blood cell flux and blood flow rate can be done, but is only practical for vessels less than ~30 μm in diameter because individual red blood cells are difficult to visualize in larger vessels due to absorption of fluorescent light by hemoglobin.

Previous methods for measuring oxygen demand in tumors include pO_2 microelectrode measurements coupled with theoretical simulations of oxygen diffusion,[16] an isolated tumor perfusion system combined with Fick's principle calculations,[17] and cryospectrophotometric microtechniques.[18] All of these methods are invasive, which makes longitudinal *in vivo* monitoring difficult. Positron emission tomography (PET) of fluoro-deoxyglucose (FDG) has also served as a valuable marker for tumor metabolism.[19,20] However, PET imaging is low resolution and expensive, and time course measurements require repeated exposure to radioisotopes.

Optical imaging of tumor oxygen supply and demand is attractive because these methods are relatively low cost, high resolution, and noninvasive, if performed in a transparent window chamber preparation. Optical imaging based on endogenous tissue contrast does not require exogenous contrast agents, and is thus well suited for long-term monitoring of cycling hypoxia in tumors. Hyperspectral imaging of hemoglobin oxygen saturation[21–23] coupled with 3-D Doppler optical coherence tomography (OCT) of calibrated microvessel blood flow rates[24–27] allow for accurate, dynamic, and noninvasive imaging of oxygen supply in tumors.[28] Doppler OCT also allows for visualization of vessel velocity profiles at any vessel cross section in the tumor, thus providing information on the shear rate on the vessel wall.[29] Oxygen demand can be optically monitored with the "redox ratio," which is the ratio of the inherent fluorescence intensity of the metabolic coenzymes FAD and NADH (the primary electron acceptor and donor, respectively, in oxidative phosphorylation.).[30] This optical redox ratio provides relative changes in the oxidation-reduction state in the cell. The redox ratio is sensitive to changes in the cellular metabolic rate and vascular oxygen supply.[30–34]

The goal of this study was to dynamically image changes in oxygen supply and demand in tumors using a novel combination of redox imaging (metabolic demand) and hyperspectral imaging, combined with Doppler OCT (oxygen supply). The results reported here are the first demonstration of combined noninvasive imaging of oxygen supply and metabolic demand in tumors *in vivo*. These data could provide insight into the sources of cycling hypoxia in tumors, and serve as the basis for further studies that will incorporate therapeutic strategies to mitigate hypoxia in tumors for improved treatment response.

2 Materials and Methods

2.1 *Multifunctional Microscope*

Fluorescence, hyperspectral, and OCT imaging were conducted on the same microscope to noninvasively monitor changes in metabolic demand and hemodynamics with tumor growth. All images were collected with a 4× objective (NA $=0.1$). Hyperspectral (hemoglobin oxygen saturation) and SDOCT (blood flow and vascular morphology) arms were connected through two separate base ports in an inverted microscope (Carl Zeiss Axiovert 200). 2-D hyperspectral images were collected with a 100-W halogen lamp for transillumination, and detection was achieved with a 10-nm bandwidth liquid crystal tunable filter (LCTF) (CRI Incorporated, Woburn, Massachusetts) placed in front of a DVC 1412 CCD camera (DVC Company, Austria, Texas).[23] Custom software was used to tune the filter and acquire images at 10-nm increments between 500 and 620 nm. Measurements of the dark offset and transmission through a neutral density filter at each wavelength were made before each imaging session. Hemoglobin saturation images were calculated by applying an extension of the Beer-Lambert law to the wavelength-dependent attenuation at each pixel (assuming oxygenated and deoxygenated hemoglobin as the primary absorbers, along with a tissue scattering parameter), and then solving for hemoglobin saturation with linear least-squares regression.[23] The system, software, and analysis techniques have previously been validated on liquid phantoms with an accuracy of approximately 1% and *in vivo*.[23]

2-D fluorescence imaging was conducted in the epi-illumination geometry with a 100-W mercury lamp. NADH images were collected with a 360-nm bandpass excitation filter (40-nm bandwidth) and a 390-nm longpass dichroic beamsplitter. FAD images were collected with a 470-nm bandpass excitation filter (40-nm bandwidth) and a 510-nm longpass dichroic beamsplitter. Fluorescence emission was collected with the same LCTF and charge-coupled device (CCD) described before for the hyperspectral arm. The LCTF was set to 480-nm and 530-nm emission for NADH and FAD imaging, respectively. Redox images were calculated by dividing the FAD image point by point by the NADH image.[30,34] To account for interanimal variability in the time-course experiments, the redox ratio for each animal was normalized the first time point of the first region of interest within each animal. Note that the redox image represents the redox ratio of a superficial (~200 to 300 μm thick) tissue layer probed by the excitation-emission wavelengths,[35] and the hemoglobin saturation images show vessels from a similarly superficial tissue layer.[22,23] OCT volumes indicate that this layer contains most of the blood vessels in the field of view. The spatial resolution of hyperspectral and redox imaging is defined by the NA of the objective ($5\ \mu m$).

The spectral domain OCT arm was illuminated by a Ti:sapphire laser source (Femtolasers, Vienna, Austria) centered at 790 nm with a 90-nm full width at half-maximum. The OCT interferometer was common path, utilizing the top surface of the window chamber cover glass as the reference reflection, and the spectral interferogram was detected using a custom-made spectrometer (spectral resolution and coverage 0.08 and 164 nm, respectively) with a 2048 element line scan CCD camera (Atmel, Aviiva, San Jose, California). The OCT system was driven by software that controls the lateral scanner and performs data acquisition and archiving (Bioptigen, Incorporated, Research Triangle park, North Carolina). 3-D blood flow images were collected with Doppler OCT, which measures phase changes due to flowing erythrocytes.[24] Phase changes were calculated from multiple A-scans collected at the same position in the volume, and were related to flow velocity profiles by measuring the angle of incidence in the 3-D volume. This method has previously been validated in flow phantoms.[36] Doppler OCT volumes were collected over a 2×1.5 mm area with 250×125 pixels (with a resulting resolution of 8 and $12\ \mu m$ in the lateral dimensions), and from 2 mm in the depth dimension with 1024 pixels, with a 1-ms integration time for each A-line. Ten repeated A-scans at each location were collected at each x-y position for Doppler shift estimation. Cross sectional vessel flow profiles were fit to a second-order polynomial and corrected for the angle of incidence to provide velocity in millimeters per second. Maximum blood velocity ($V_{\max}$) was determined from the peak of this fit, vessel diameter (D) was determined from the zero-crossings of the fit, and the shear rate on the vessel wall was determined from the derivative of the fit (dv_z/dr) evaluated at the vessel wall, assuming a Newtonian fluid.[29] Note that in vessels with diameters 30 to $60\ \mu m$, the velocity profile is expected to be blunter than a parabola (this reflects the non-continuum behavior of blood rather than non-Newtonian behavior).[25,37–39] Thus, the estimated wall shear rate may be an underestimate in these calculations. However, our fit results suggest that the departure from a parabola is small, so the second-order polynomial fit is a reasonable approximation. The flow in the vessel is the average velocity in the vessel times the cross sectional area of the vessel $[V_{\max}/2^*\pi^*(D/2)^2]$.

2.2 *In Vivo Imaging*

All *in vivo* experiments were conducted under a protocol approved by the Duke University Institutional Animal Care and Use Committee. A titanium window chamber was surgically implanted under anesthesia (ketamine 100 mg/kg and xylazine 10 mg/kg IP) on the back of athymic nude mice (nu/nu, NCI, Frederick, Maryland). A window chamber tumor was established during chamber implantation by injecting $20\ \mu L$ of a single cell suspension (8×10^6 cells) of FaDu (human squamous cell carcinoma) cells into the dorsal skin fold prior to placing a 12-mm-diam number 2 round glass coverslip (Erie Scientific, Portsmouth, New Hampshire) over the exposed tissue. Animals were housed in an on-site housing facility with *ad libitum* access to food and water and standard 12-h light/dark cycles.

Redox and hemoglobin saturation imaging were validated on mice with a tumor-free window chamber. Perturbation experiments were performed with the mice under ketamine/ xylazine anesthesia (maintained at body temperature) while breathing air, then 100% oxygen through a nose cone, and then 100% nitrogen through a nose cone at 1-L/min flow rate.

For longitudinal imaging of tumor growth, animals were anesthetized with Isoflurane (1.5% with oxygen) and maintained at body temperature. Imaging began when tumors reached 1 to 2 mm in diameter. A Doppler OCT volume (5-min acquisition), followed by hemoglobin saturation (30-s acquisition) and redox (15-sec acquisition) imaging were collected every 6 h for 36 h. Vessel morphology maps were used to achieve spatial registration between each imaging session. Transition between microscope modes was approximately 1 min. Mice were allowed to recover after each imaging session.

Note that no corrections were made to the data to account for the cardiac cycle. All vessels of interest were microvessels (diameter $<70\ \mu m$) that do not exhibit large changes in flow due to the cardiac cycle. Previous studies have used Fourier analysis of blood flow and pO_2 in rats to show low-frequency fluctuations (<2 cycles/min) in both tumor and muscle tissues, which is much lower than the measured respiration rate and heart rate (~50 to 60 and 300 to 400 cycles/min, respectively.[7]

2.3 *Statistical Analysis*

Doppler OCT and hyperspectral data were collected over the 36-h time course from a total of five mice, and redox images were also collected over the time course from three of these mice. Three to six regions of interest were chosen within each tumor based on visual inspection of the hemoglobin saturation time course images. Vessel regions that demonstrated fluctuations in hemoglobin saturation over the time course, and that were spatially distributed across the surface of the tumor, were chosen as regions of interest. The mean and standard deviation of the hemoglobin saturation were measured at these vessel regions of interest, over an area within the inner diameter of the vessel and a slab thickness of no more than 20- μm. The Doppler velocity profile was measured at the same vessel cross section of interest. The mean and standard deviation of the redox ratio was measured from a 25 to 60-μm-diam circular area adjacent to the vessel. The redox area of interest was chosen to exclude blood vessels and to remain less than $100\ \mu m$ in diameter (the length of oxygen diffusion in tissue.[40] A total of 21 regions of interest were analyzed over the time course, with 14 regions of interest that include redox ratio measurements. One of the animals for which redox images were collected included only six time points for the four regions of interest within that animal, due to tumor hemorrhage at the last time point.

Pearson's correlation coefficients were used to determine linear correlations between blood oxygenation (hemoglobin saturation), blood flow (maximum velocity, flow, vessel inner diameter, and shear rate), and metabolic demand (redox ratio). Significant correlations ($p < 0.05$) are reported for the pooled data (all regions of interest and time points grouped together), for which there were $n=143$ samples for the blood oxygenation and blood flow comparisons, and $n=94$ samples for the metabolic demand comparisons. As described before, the redox ratio was normalized to the first time point of the first region of interest within each animal. Thus, blood oxygenation and blood flow biomarkers were also normalized to the first time point of the first region of interest within each animal for comparisons with the redox ratio only.

Next, a linear mixed model was used to analyze repeated measures. This approach separates the interanimal variation from the total variation (thus increasing statistical power) to determine whether the biomarkers (i.e., hemoglobin saturation, redox ratio, maximum velocity, vessel inner diameter, flow, and shear rate) change over time. Let Y_{ijk} denote the value of a biomarker from the i'th animal in the j'th region of interest (ROI) at the k'th time point. Assume Y_{ijk} follows the linear mixed model $Y_{ijk}=\mu+t_k+b_{ij}+\varepsilon_{ijk}$ (model 1); where $\mu+t_k$ is the time effect, b_{ij} is the animal specific random effect, and ε_{ijk} are intra-animal errors. The time effect was tested by the F-statistic. A second mixed model was used to address the association of two variables adjusting for the covariate time. Model 2 ($Y_{ijk}=\mu+X_{ijk}+t_k+b_{ij}+\varepsilon_{ijk}$) includes the covariate X, and the linear association of biomarker X on the behavior of another biomarker Y was tested with the F-statistic. Associations were tested between blood oxygenation (hemoglobin saturation), blood flow (maximum velocity, flow, vessel inner diameter, and shear rate), and metabolic demand (redox ratio) biomarkers.

3 Results

The results of perturbation experiments in a normal mouse window chamber (no tumor cells were injected) are shown in Fig. 1. To segment the vessels from background, the hemoglobin saturation images were thresholded by the total absorption image. The same mask was negatively applied to the redox images. Note that there are two distinct peaks in the hemoglobin saturation histogram for air and oxygen breathing [Fig. 1(b)], due to arteriolar and venous blood oxygenation. Nitrogen and oxygen breathing resulted in a decrease and increase, respectively, in both the redox ratio and the hemoglobin saturation compared to air breathing, as expected. The results in Fig. 1 were confirmed in a second mouse, and are consistent with previous reports.[23,33] These perturbation experiments indicate that NADH and FAD signals have been properly isolated for redox imaging.

The hemoglobin saturation [Fig. 1(a)] and redox [Fig. 1(b)] images collected from one mouse over the 36-h time course are shown in Fig. 2. Longitudinal oxygen gradients are apparent in the hemoglobin saturation images, with decreased hemoglobin saturation levels within the tumor [Fig. 2(a), at the 1] compared with the tumor periphery [Fig. 2(a), at the 2]. These longitudinal gradients have been previously observed in studies employing phosphorescence lifetime imaging of pO_2.[41,42] The redox images indicate that the redox ratio within the tumor is higher in areas with large-diameter oxygenated vessels [Fig. 2(b), at the 3]. Both the hemoglobin saturation and the redox ratio appear to vary with time.

Figure 3 shows an en-face view of the 3-D Doppler OCT volume (manually segmented in Amira software, Mercury Systems, Chelmsford, Massachusetts) from the zero-hour time point [Fig. 3(a)] of the same animal shown in Fig. 2. Plots of the cross sectional vessel velocity profile from one vessel [arrow, Fig. 3(a)] are shown along with the second-order polynomial fit and the R-squared value of the fit for each time point [Figs. 3(b)–3(h)]. The shape and peak of the velocity profile changes with time, indicating changes in vessel diameter, shear rate, and maximum vessel velocity over the 36-h time course.

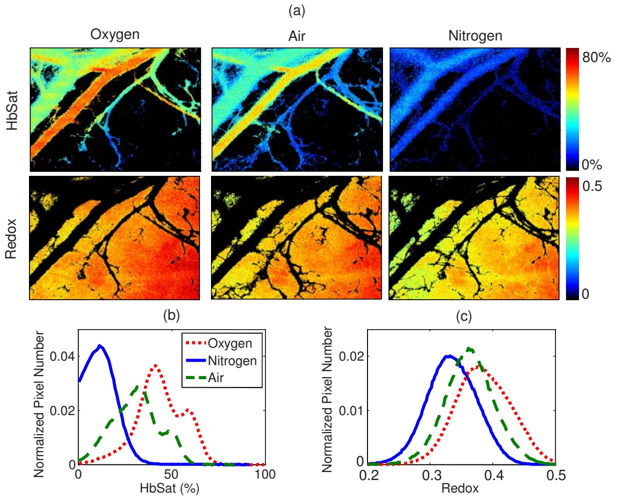

Fig. 1 Hemoglobin saturation (HbSat) and redox images taken from a nontumor-bearing window chamber of a mouse breathing oxygen, air, and nitrogen (a) at 1 L/min through a nose cone. To segment the vessels from background, the hemoglobin saturation images were thresholded by the total absorption image. The same mask was negatively applied to the redox images. Histograms of (b) the hemoglobin saturation and (c) redox images show that the hemoglobin saturation and redox ratio increase with oxygen breathing and decrease with nitrogen breathing, as expected. Image sizes are 2×1.5 mm.

Figure 4 shows quantitative measures of the redox ratio [Fig. 4(b)], hemoglobin saturation [Fig. 4(c)], vessel maximum velocity [Fig. 4(d)], vessel inner diameter [Fig. 4(e)], flow [Fig. 4(f)], and shear rate [Fig. 4(g)] over the 36-h time course in six regions of interest [Fig. 4(a)] from the same animal shown in Figs. 2 and 3. These plots indicate that all variables change with time within the same region of interest within the same animal. All regions of interest appear to vary together with time for the redox ratio [Fig. 4(b)] and for the hemoglobin saturation [Fig. 4(c)]. However, each region of interest appears to vary differently with time compared with the other five regions of interest for the blood flow parameters [Figs. 4(d)–4(g)].

The spatial distribution of the redox ratio with respect to the nearest vessel is shown in Fig. 5 for tumors and normal tissues. There is a significant ($p<0.05$) decrease in the redox ratio for points greater than 30 μm from the nearest vessel, compared to the point closest to the nearest vessel (point zero). This is in agreement with previous reports that measured pO_2 as a function of distance from the nearest vessel.[15,16] However, the normal tissues showed no significant increase or decrease in the redox ratio as a function of distance from the nearest vessel.

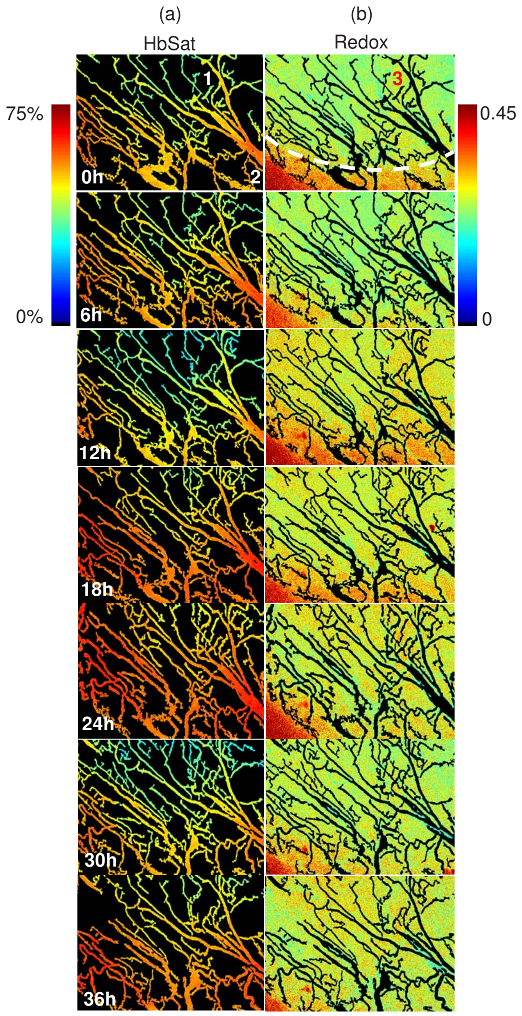

Fig. 2 (a) Hemoglobin saturation and (b) redox images taken from one mouse over the 36-h time course. The time of imaging in hours is indicated in the lower left corner of each hemoglobin saturation image. For the purposes of this figure only, the hemoglobin saturation images were thresholded by the total absorption image, and then by a 15-μm-diam circular kernel. The kernel excluded pixels with an absorption value smaller than the average of the 15-μm-diam kernel. The mask was applied to hemoglobin saturation images to isolate vessels from the nonvascular background, and the same vessel mask was negatively applied to the redox images. The tumor boundary is indicated by a white dashed line in (b). Image sizes are 2×1.5 mm.

The relationship between the biomarkers for blood oxygenation (hemoglobin saturation), blood flow (maximum velocity, flow, vessel inner diameter, and shear rate), and metabolic demand (redox ratio) were tested with the Pearson's correlation coefficient (Table 1) for the pooled data (all regions of interest and time points from all animals grouped together). The correlation coefficients (r) in Table 1 are shown for biomarker relationships for which a significant ($p < 0.05$) linear correlation was found. The hemoglobin saturation is positively correlated with the maximum velocity, flow, and shear rate (HbSat line of Table 1), and the redox ratio is positively correlated with the hemoglobin saturation, maximum velocity, flow, and diameter. All statistically significant correlations are weak ($r \leqslant 0.5$), which indicates that many factors contribute to the variability of each biomarker, as expected.[11] The linear mixed model determined that all biomarkers significantly change ($p < 0.05$) with time (Fig. 6), and that the vessel diameter is associated with the redox ratio of the adjacent tissue ($p < 0.05$) after adjusting for the effect of time. No other biomarker pairs were found to have significant associations ($p > 0.05$) when adjusting for the effect of time.

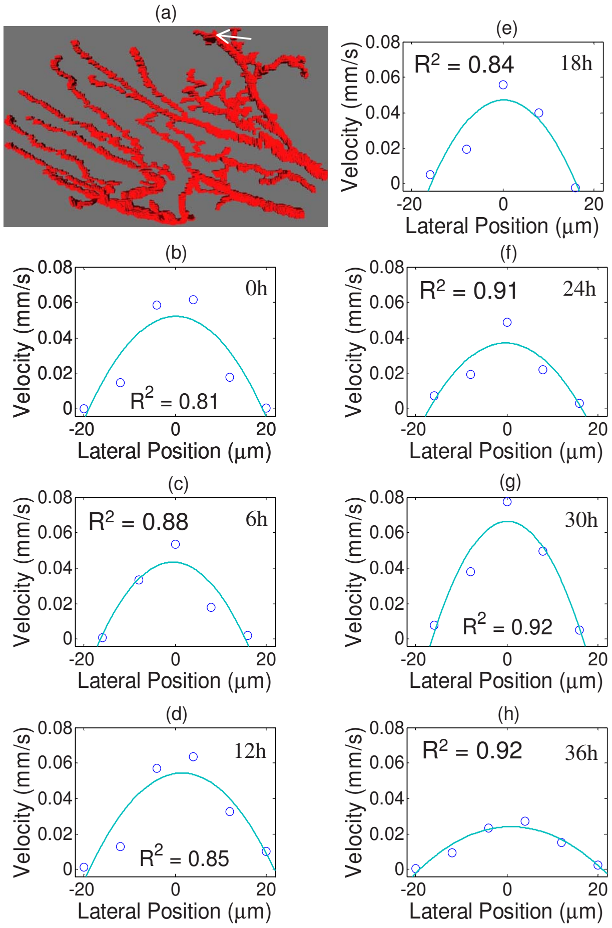

Fig. 3 An en-face view of the 3-D Doppler OCT volume (manually segmented in Amira software, Mercury Systems) from (a) the zero-hour time point of the same animal shown in Fig. 2 (2×1.5-mm imaged area, 0.6 mm depth). Plots of the cross sectional vessel velocity profile from one vessel [arrow in (a)] are shown along with the second-order polynomial fit and the R-squared value of the fit for each time point (b) through (h). The time of imaging in hours is indicated in the upper right corner of each plot.

4 Discussion

Multifunctional optical imaging of oxygen supply and demand has several advantages over traditional techniques. The combination of OCT, absorption, and fluorescence imaging provides quantitative information on blood flow, blood oxygenation, and metabolic demand, respectively, in living tissues. This combination of optical imaging modalities is noninvasive, relatively inexpensive, and fast. These attributes are well suited for long-term repeated measures *in vivo*. We have demonstrated the attributes of this imaging platform for the study of cycling hypoxia in tumors in the dorsal skin fold mouse window chamber. This is the first demonstration of

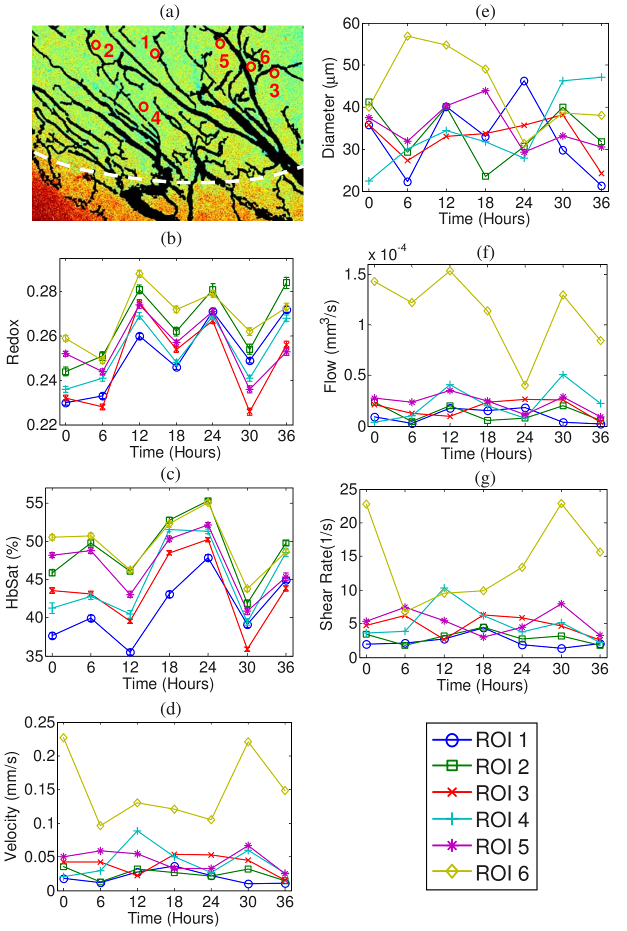

Fig. 4 Quantitative measures of (b) the redox ratio, (c) hemoglobin saturation, (d) vessel maximum velocity, (e) vessel inner diameter, (f) flow, and (g) shear rate over the 36-h time course in (a) six regions of interest from the same animal shown in Figs. 2 and 3. The mean and standard error are plotted for (b) the redox ratio and (c) hemoglobin saturation, and the mean (d) through (g) is plotted for the remaining variables.

combined noninvasive monitoring of oxygen supply and metabolic demand in tumors *in vivo*.

All biomarkers (hemoglobin saturation, redox ratio, maximum velocity, vessel inner diameter, flow, and shear rate) significantly changed with time ($p<0.05$) over the 36-h imaging period, which supports previous reports that blood oxygenation, blood flow, and metabolic demand all contribute to cycling hypoxia in tumors.[3] These variations in oxygen supply and demand are superimposed on a decline in metabolic demand with distance from the nearest vessel in tumors (Fig. 5), in agreement with previous interstitial pO_2 microelectrode measurements.[15,16] Our results indicate a positive correlation between the blood flow, blood oxygenation, and metabolic demand in tumors (Table 1), but the correlation between these biomarkers is weak and suggests that no single biomarker can fully explain the behavior of another.[11] When adjusting for the effect of time, the vessel diameter was found to be associated with the redox ratio of the adjacent tissue, which indicates that vessel diameter plays a key role in tumor metabolic activity and cycling hypoxia in tumors.[43] Future studies will exploit these biomarkers to investigate functional changes in oxygen supply and demand in response to therapeutic strategies. For example, it is possible that antiangiogenic therapies may stabilize cycling hypoxia by reducing the magnitude of changes in vascular diameter and blood flow rate over time.[3] It is anticipated, however, that antiangiogenic therapies would have less influence on redox ratio. The combination of technologies presented here would permit a direct test of this hypothesis.

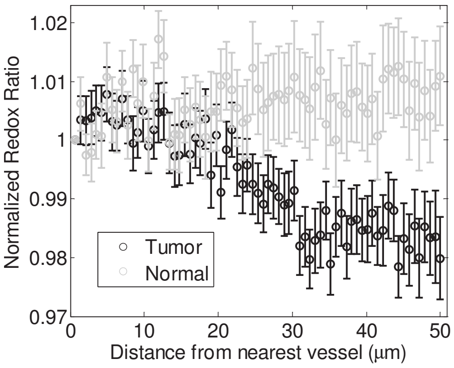

Fig. 5 Normalized redox ratio as a function of distance from the nearest vessel for tumors (compiled from $n=94$ line profiles corresponding to the 94 regions of interest from the three redox animals across the entire tumor time course), and for normal tissues (compiled from $n=36$ line profiles from six regions of interest from each of six normal animals). All profiles were normalized to the point closest to the vessel before averaging across all line profiles. For the tumors, there is a significant ($p<0.05$) decrease in the redox ratio between the point closest to the vessel (point zero) and all points greater than 30 μm from point zero. Normal tissues did not show a significant increase or decrease in the redox ratio as a function of the distance from the nearest vessel. Error bars are standard error.

Extracted biomarkers including the hemoglobin saturation,[44,45] maximum velocity and vessel diameter,[14] and shear rate,[46] are all in qualitative agreement with previous studies that employed different techniques in window chamber tumors, as well as a previous study that employed the same techniques in a different window chamber tumor model.[28] Variations in red blood cell flux and pO_2,[15] hemoglobin oxygen saturation,[23] and diameter[44] have previously

Table 1 Pearson correlation coefficients for hemoglobin saturation (HbSat) versus maximum velocity ($V_{\max}$), flow, diameter, and shear rate (top line) and for the normalized redox ratio, normalized hemoglobin saturation, normalized maximum velocity, normalized flow, normalized diameter and normalized shear rate (bottom line). The data are compiled from all regions of interest and time points grouped together, with $n=143$ observations for the top line and $n=94$ observations for the bottom line. The correlation coefficient is listed for comparisons with $p<0.05$.

	$V_{\max}$ (mm/s)	Flow (mm^3/s)		Diameter (μm)	Shear rate (1/s)
HbSat (%)	0.49	0.37		$p>0.05$	0.49
	HbSat	$V_{\max}$	Flow	Diameter	Shear rate
Redox	0.50	0.28	0.32	0.43	$p>0.05$

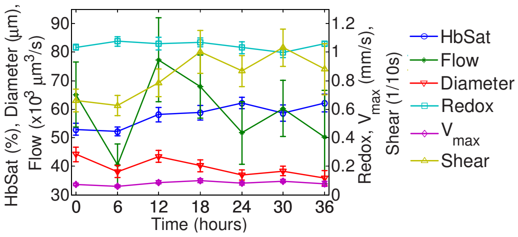

Fig. 6 Longitudinal variations in all biomarkers as a function of time. Values at each time point were averaged across all regions of interest and animals for the hemoglobin saturation (HbSat), flow, diameter, maximum velocity (V_{max}), and shear rate ($n=21$), as well as for the redox ratio ($n=14$). Note that the 36-h time point has four fewer samples (see Sec. 2). The linear mixed model determined that all biomarkers significantly change ($p<0.05$) with time, and that the vessel diameter is associated with the redox ratio of the adjacent tissue ($p<0.05$) after adjusting for the effect of time. Error bars are standard error.

been observed in window chamber tumors over time scales ranging from one hour to several days.

Previous studies have employed different methods to investigate the relationship between some of the biomarkers presented in this work. Intravascular pO_2 and blood flow rate, as well as interstitial pO_2 and red blood cell velocity or vessel diameter, were found to have no correlation in a previous study.[13] Helmlinger et al. used phosphorescence lifetime imaging to quantify pO_2 and video microscopy to quantify red blood cell velocity and vessel diameter. Although hemoglobin oxygen saturation and pO_2 are related, they are not the same endpoint, and video microscopy provides a 2-D projection rather than an absolute measure of blood velocity. The study design and tumor models employed in the previous and current studies also differ. Previous studies employing the same techniques as the current study have found a significant correlation between the hemoglobin saturation and blood velocity, blood flow, and shear rate in a different tumor model.[28] Additional studies[15] indicate that vessel remodeling with tumor growth alters flow distributions, and the relationship between blood flow and tissue oxygenation in tumors is heterogeneous.

Demand for oxygen in tumor cells is created by the normal respirative process of the cells.[32] The redox ratio is a measure of cell respiration (oxygen demand),[30] while the hemoglobin oxygen saturation is one component of oxygen supply. Therefore, it is intuitive that the hemoglobin saturation of a vessel is somewhat related to the redox ratio of the surrounding tissue. However, we do not expect a one-to-one correlation between the redox ratio and hemoglobin saturation. Oxygen delivery is affected by the hemoglobin saturation as well as the vascular architecture, hematocrit, and blood flow.[32] The redox ratio is indicative of changes in oxygen supply as well as metabolite availability and mitochondrial membrane potential.[47] Thus, the redox ratio, blood flow and hemoglobin saturation provide complementary information.

Figure 5 shows a decrease in the redox ratio with increasing distance from the nearest vessel in tumors, and no such decrease in the redox ratio with distance from the nearest vessel in normal tissues. We hypothesize that this tumor gradient is due to increased metabolic activity coupled with compromised microvascular oxygen transport in tumors compared to normal tissues. Future studies will investigate this hypothesis.

In this study, absorption and fluorescence microscopy were combined with OCT to unravel the contributions of blood flow, blood oxygenation, and metabolic demand on cycling hypoxia. These findings could guide the design and development of therapeutic strategies to mitigate cycling hypoxia, and thus reduce tumor resistance to radiation and chemotherapies. Second, this study experimentally demonstrates the attributes of our multifunctional optical imaging approach for mapping oxygen supply and demand *in vivo*. This approach has broad applicability in the study of other diseases that are affected by oxygen supply and demand, such as cerebral hypoxia (stroke), cardiac ischemia, and Alzheimer's disease. Moreover, these processes can be studied with multifunctional optical imaging *in vivo* and do not require contrast-enhancing dyes.

Acknowledgments

The authors would like to thank Greg Palmer and Hansford Hendargo for their technical expertise. This research was supported by NIH/NCI CA40355, NIH EB006338, and NIH 014743. Author Skala acknowledges fellowship support through the NIH/NCI (F32 CA130309). Joseph Izatt has a financial interest in Bioptigen, Inc. as Chief Technology Officer.

References

1. J. M. Brown and W. R. Wilson, "Exploiting tumour hypoxia in cancer treatment," *Nature Rev.* **4**(6), 437–447 (2004).
2. P. Vaupel and A. Mayer, "Hypoxia in cancer: significance and impact on clinical outcome," *Cancer Metastasis Rev.* **26**(2), 225–239 (2007).
3. M. W. Dewhirst, Y. Cao, and B. Moeller, "Cycling hypoxia and free radicals regulate angiogenesis and radiotherapy response," *Nature Rev.* **8**(6), 425–437 (2008).
4. M. W. Dewhirst, "Intermittent hypoxia furthers the rationale for hypoxia-inducible factor-1 targeting," *Cancer Res.* **67**(3), 854–855 (2007).
5. L. I. Cardenas-Navia, D. Yu, R. D. Braun, D. M. Brizel, T. W. Secomb, and M. W. Dewhirst, "Tumor-dependent kinetics of partial pressure of oxygen fluctuations during air and oxygen breathing," *Cancer Res.* **64**(17), 6010–6017 (2004).
6. K. G. Brurberg, H. K. Skogmo, B. A. Graff, D. R. Olsen, and E. K. Rofstad, "Fluctuations in pO2 in poorly and well-oxygenated spontaneous canine tumors before and during fractionated radiation therapy," *Radiol. Oncol.* **77**(2), 220–226 (2005).
7. R. D. Braun, J. L. Lanzen, and M. W. Dewhirst, "Fourier analysis of fluctuations of oxygen tension and blood flow in R3230Ac tumors and muscle in rats," *Am. J. Physiol.* **277**(2 Pt 2), H551–568 (1999).
8. K. G. Brurberg, B. A. Graff, and E. K. Rofstad, "Temporal heterogeneity in oxygen tension in human melanoma xenografts," *Br. J. Cancer* **89**(2), 350–356 (2003).
9. G. L. Semenza, "Targeting HIF-1 for cancer therapy," *Nature Rev.* **3**(10), 721–732 (2003).
10. H. Kimura, R. D. Braun, E. T. Ong, R. Hsu, T. W. Secomb, D. Papahadjopoulos, K. Hong, and M. W. Dewhirst, "Fluctuations in red cell flux in tumor microvessels can lead to transient hypoxia and reoxygenation in tumor parenchyma," *Cancer Res.* **56**(23), 5522–5528 (1996).
11. T. W. Secomb, R. Hsu, E. T. Ong, J. F. Gross, and M. W. Dewhirst, "Analysis of the effects of oxygen supply and demand on hypoxic fraction in tumors," *Acta Oncol.* **34**(3), 313–316 (1995).
12. K. O. Hicks, F. B. Pruijn, T. W. Secomb, M. P. Hay, R. Hsu, J. M. Brown, W. A. Denny, M. W. Dewhirst, and W. R. Wilson, "Use of three-dimensional tissue cultures to model extravascular transport and predict *in vivo* activity of hypoxia-targeted anticancer drugs," *J. Natl. Cancer Inst.* **98**(16), 1118–1128 (2006).
13. G. Helmlinger, F. Yuan, M. Dellian, and R. K. Jain, "Interstitial pH

and pO2 gradients in solid tumors *in vivo*: high-resolution measurements reveal a lack of correlation," *Nat. Med.* **3**(2), 177–182 (1997).

14. M. W. Dewhirst, R. Oliver, C. Y. Tso, C. Gustafson, T. Secomb, and J. F. Gross, "Heterogeneity in tumor microvascular response to radiation," *Int. J. Radiat. Oncol., Biol., Phys.* **18**(3), 559–568 (1990).
15. J. Lanzen, R. D. Braun, B. Klitzman, D. Brizel, T. W. Secomb, and M. W. Dewhirst, "Direct demonstration of instabilities in oxygen concentrations within the extravascular compartment of an experimental tumor," *Cancer Res.* **66**(4), 2219–2223 (2006).
16. M. W. Dewhirst, T. W. Secomb, E. T. Ong, R. Hsu, and J. F. Gross, "Determination of local oxygen consumption rates in tumors," *Cancer Res.* **54**(13), 3333–3336 (1994).
17. P. Vaupel, K. Ostheimer, and W. Muller-Klieser, "Circulatory and metabolic responses of malignant tumors during localized hyperthermia," *J. Cancer Res. Clin. Oncol.* **98**(1), 15–29 (1980).
18. P. Vaupel, F. Kallinowski, and P. Okunieff, "Blood flow, oxygen and nutrient supply, and metabolic microenvironment of human tumors: a review," *Cancer Res.* **49**(23), 6449–6465 (1989).
19. L. K. Shankar, J. M. Hoffman, S. Bacharach, M. M. Graham, J. Karp, A. A. Lammertsma, S. Larson, D. A. Mankoff, B. A. Siegel, A. Van den Abbeele, J. Yap, and D. Sullivan, "Consensus recommendations for the use of 18F-FDG PET as an indicator of therapeutic response in patients in National Cancer Institute Trials," *J. Nucl. Med.* **47**(6), 1059–1066 (2006).
20. P. Som, H. L. Atkins, D. Bandoypadhyay, J. S. Fowler, R. R. MacGregor, K. Matsui, Z. H. Oster, D. F. Sacker, C. Y. Shiue, H. Turner, C. N. Wan, A. P. Wolf, and S. V. Zabinski, "A fluorinated glucose analog, 2-fluoro-2-deoxy-D-glucose (F-18): nontoxic tracer for rapid tumor detection," *J. Nucl. Med.* **21**(7), 670–675 (1980).
21. C. Dedeugd, M. Wankhede, and B. S. Sorg, "Multimodal optical imaging of microvessel network convective oxygen transport dynamics," *Appl. Opt.* **48**(10), D187–197 (2009).
22. B. S. Sorg, M. E. Hardee, N. Agarwal, B. J. Moeller, and M. W. Dewhirst, "Spectral imaging facilitates visualization and measurements of unstable and abnormal microvascular oxygen transport in tumors," *J. Biomed. Opt.* **13**(1), 014026 (2008).
23. B. S. Sorg, B. J. Moeller, O. Donovan, Y. Cao, and M. W. Dewhirst, "Hyperspectral imaging of hemoglobin saturation in tumor microvasculature and tumor hypoxia development," *J. Biomed. Opt.* **10**(4), 44004 (2005).
24. J. A. Izatt, M. D. Kulkarni, S. Yazdanfar, J. K. Barton, and A. J. Welch, "*In vivo* bidirectional color Doppler flow imaging of picoliter blood volumes using optical coherence tomography," *Opt. Lett.* **22**(18), 1439–1441 (1997).
25. J. Moger, S. J. Matcher, C. P. Winlove, and A. Shore, "Measuring red blood cell flow dynamics in a glass capillary using Doppler optical coherence tomography and Doppler amplitude optical coherence tomography," *J. Biomed. Opt.* **9**(5), 982–994 (2004).
26. M. Khurana, E. H. Moriyama, A. Mariampillai, and B. C. Wilson, "Intravital high-resolution optical imaging of individual vessel response to photodynamic treatment," *J. Biomed. Opt.* **13**(4), 040502 (2008).
27. V. X. Yang, S. J. Tang, M. L. Gordon, B. Qi, G. Gardiner, M. Cirocco, P. Kortan, G. B. Haber, G. Kandel, I. A. Vitkin, B. C. Wilson, and N. E. Marcon, "Endoscopic Doppler optical coherence tomography in the human GI tract: initial experience," *Gastrointest. Endosc.* **61**(7), 879–890 (2005).
28. M. C. Skala, A. Fontanella, H. Hendargo, M. W. Dewhirst, and J. A. Izatt, "Combined hyperspectral and spectral domain optical coherence tomography microscope for noninvasive hemodynamic imaging," *Opt. Lett.* **34**(3), 289–291 (2009).
29. T. G. van Leeuwen, M. D. Kulkarni, S. Yazdanfar, A. M. Rollins, and J. A. Izatt, "High-flow-velocity and shear-rate imaging by use of color Doppler optical coherence tomography," *Opt. Lett.* **24**(22), 1584–1586 (1999).
30. B. Chance, B. Schoener, R. Oshino, F. Itshak, and Y. Nakase, "Oxidation-reduction ratio studies of mitochondria in freeze-trapped samples. NADH and flavoprotein fluorescence signals," *J. Biol. Chem.* **254**(11), 4764–4771 (1979).
31. R. Drezek, C. Brookner, I. Pavlova, I. Boiko, A. Malpica, R. Lotan, M. Follen, and R. Richards-Kortum, "Autofluorescence microscopy of fresh cervical-tissue sections reveals alterations in tissue biochemistry with dysplasia," *Photochem. Photobiol.* **73**(6), 636–641 (2001).
32. C. J. Gulledge and M. W. Dewhirst, "Tumor oxygenation: a matter of supply and demand," *Anticancer Res.* **16**(2), 741–749 (1996).
33. N. Ramanujam, R. R. Kortum, S. Thomsen, A. M. Jansen, M. Follen, and B. Chance, "Low temperature fluorescence imaging of freeze-trapped human cervical tissues," *Opt. Express* **8**, 335–343 (2001).
34. M. C. Skala, K. M. Riching, A. Gendron-Fitzpatrick, J. Eickhoff, K. W. Eliceiri, J. G. White, and N. Ramanujam, "*In vivo* multiphoton microscopy of NADH and FAD redox states, fluorescence lifetimes, and cellular morphology in precancerous epithelia," *Proc. Natl. Acad. Sci. U.S.A.* **104**(49), 19494–19499 (2007).
35. N. Ramanujam, "Fluorescence spectroscopy of neoplastic and non-neoplastic tissues," *Neoplasia* **2**(1–2), 89–117 (2000).
36. A. Davis, J. Izatt, and F. Rothenberg, "Quantitative measurement of blood flow dynamics in embryonic vasculature using spectral Doppler velocimetry," *Anat. Rec.* **292**(3), 311–319 (2009).
37. P. Bagchi, "Mesoscale simulation of blood flow in small vessels," *Biophys. J.* **92**(6), 1858–1877 (2007).
38. J. J. Bishop, P. R. Nance, A. S. Popel, M. Intaglietta, and P. C. Johnson, "Effect of erythrocyte aggregation on velocity profiles in venules," *Am. J. Physiol.* **280**(1), H222–236 (2001).
39. M. Sharan and A. S. Popel, "A two-phase model for flow of blood in narrow tubes with increased effective viscosity near the wall," *Biorheology* **38**(5–6), 415–428 (2001).
40. K. Groebe and P. Vaupel, "Evaluation of oxygen diffusion distances in human breast cancer xenografts using tumor-specific *in vivo* data: role of various mechanisms in the development of tumor hypoxia," *Int. J. Radiat. Oncol., Biol., Phys.* **15**(3), 691–697 (1988).
41. M. W. Dewhirst, E. T. Ong, R. D. Braun, B. Smith, B. Klitzman, S. M. Evans, and D. Wilson, "Quantification of longitudinal tissue pO2 gradients in window chamber tumours: impact on tumour hypoxia," *Br. J. Cancer* **79**(11–12), 1717–1722 (1999).
42. K. Erickson, R. D. Braun, D. Yu, J. Lanzen, D. Wilson, D. M. Brizel, T. W. Secomb, J. E. Biaglow, and M. W. Dewhirst, "Effect of longitudinal oxygen gradients on effectiveness of manipulation of tumor oxygenation," *Cancer Res.* **63**(15), 4705–4712 (2003).
43. A. R. Pries, A. J. M. Cornelissen, A. A. Sloot, M. Hinkeldey, M. R. Dreher, M. Höpfner, M. W. Dewhirst, and T. W. Secomb, "Structural adaptation and heterogeneity of normal and tumor microvascular networks," *PLOS Comput. Biol.* **5**(5), e1000394 (2009).
44. M. W. Dewhirst, H. Kimura, S. W. Rehmus, R. D. Braun, D. Papahadjopoulos, K. Hong, and T. W. Secomb, "Microvascular studies on the origins of perfusion-limited hypoxia," *Br. J. Cancer* **27**, S247–251 (1996).
45. B. R. Duling and R. M. Berne, "Longitudinal gradients in periarteriolar oxygen tension. A possible mechanism for the participation of oxygen in local regulation of blood flow," *Circ. Res.* **27**(5), 669–678 (1970).
46. Y. Tsuzuki, D. Fukumura, B. Oosthuyse, C. Koike, P. Carmeliet, and R. K. Jain, "Vascular endothelial growth factor (VEGF) modulation by targeting hypoxia-inducible factor-1alpha--〉 hypoxia response element--〉 VEGF cascade differentially regulates vascular response and growth rate in tumors," *Cancer Res.* **60**(22), 6248–6252 (2000).
47. G. M. Palmer, R. J. Viola, T. Schroeder, P. S. Yarmolenko, M. W. Dewhirst, and N. Ramanujam, "Quantitative diffuse reflectance and fluorescence spectroscopy: tool to monitor tumor physiology *in vivo*," *J. Biomed. Opt.* **14**(2), 024010 (2009).

Journal of Biomedical Optics 15(6), 066021 (November/December 2010)

Optical imaging of tumor hypoxia dynamics

Gregory M. Palmer
Duke University Medical Center
Department of Radiation Oncology
P.O. Box 3455
Durham, North Carolina 27710

Andrew N. Fontanella
Duke University
Department of Biomedical Engineering
P.O. Box 3455
Durham, North Carolina 27710

Guoqing Zhang
University of Virginia
Department of Chemistry
P.O. Box 400319
Charlottesville, Virginia 22904

Gabi Hanna
Duke University Medical Center
Department of Radiation Oncology
P.O. Box 3455
Durham, North Carolina 27710

Cassandra L. Fraser
University of Virginia
Department of Chemistry
P.O. Box 400319
Charlottesville, Virginia 22904

Mark W. Dewhirst
Duke University Medical Center
Department of Radiation Oncology
and
Duke University
Department of Biomedical Engineering
P.O. Box 3455
Durham, North Carolina 27710

Abstract. The influence of the tumor microenvironment and hypoxia plays a significant role in determining cancer progression, treatment response, and treatment resistance. That the tumor microenvironment is highly heterogeneous with significant intratumor and intertumor variability presents a significant challenge in developing effective cancer therapies. Critical to understanding the role of the tumor microenvironment is the ability to dynamically quantify oxygen levels in the vasculature and tissue in order to elucidate the roles of oxygen supply and consumption, spatially and temporally. To this end, we describe the use of hyperspectral imaging to characterize hemoglobin absorption to quantify hemoglobin content and oxygen saturation, as well as dual emissive fluorescent/phosphorescent boron nanoparticles, which serve as ratiometric indicators of tissue oxygen tension. Applying these techniques to a window-chamber tumor model illustrates the role of fluctuations in hemoglobin saturation in driving changes in tissue oxygenation, the two being significantly correlated ($r = 0.77$). Finally, a green-fluorescence-protein reporter for hypoxia inducible factor-1 (HIF-1) provides an endpoint for hypoxic stress in the tumor, which is used to demonstrate a significant association between tumor hypoxia dynamics and HIF-1 activity in an *in vivo* demonstration of the technique. *© 2010 The International Society for Optical Engineering.* [DOI: 10.1117/1.3523363]

Keywords: hyperspectral imaging; microscopy; phosphorescense; absorption; flourescence; image processing.

Paper 10376R received Jul. 9, 2010; revised manuscript received Oct. 6, 2010; accepted for publication Oct. 7, 2010; published online Dec. 20, 2010.

Tumor hypoxia plays an important role in cancer progression, metastasis, and the effectiveness of therapies.[1–3] It is a highly dynamic process and the temporal dynamics can play a significant role in treatment resistance and tumor aggressiveness.[2,4–10] A recent trend in therapeutic strategies is to target tumor angiogenesis in order to modify the microenvironment and make tumors more sensitive to conventional therapies.[11] The ability to measure pO_2 and image tumor hypoxia on the microscopic level is essential to further understanding microenvironmental factors and modifying therapies, depending on treatment response. Characterizing the local microenvironment, particularly hypoxia, longitudinally, on a microscopic scale would be ideal. This is a challenging problem, however, and one for which no established imaging technique exists. Many methods have been developed that range from histological staining with reducible nitroimidazole reagents, protein markers, and green fluorescence protein (GFP) or luciferase reporter genes, to electrochemical probe methods, and optical, nuclear medicine, and magnetic resonance techniques[12] although some methods are only suitable for the laboratory, others have been translated into the clinic, and all have their advantages and drawbacks.[13,14] The key point is that there is no easily implemented technique for imaging vascular oxygenation (hemoglobin oxygenation) in combination with tissue oxygen tension on the microcirculatory level. We present an approach based on hyperspectral imaging of hemoglobin absorption and dual emissive boron nanoparticles (BNPs). The combination of these techniques enables quantification of both oxygen supply (hemoglobin oxygen saturation) and tissue oxygen tension (BNPs ratiometric sensing).

Address all correspondence to: Gregory M. Palmer, Duke University, Department of Radiation Oncology, 288 MSRB 1, 203 Research Drive, P.O. Box 3455, Durham, North Carolina 27710; Tel: 919-613-5053; Fax: 919-684-8718; E-mail: greg.palmer@duke.edu

1083-3668/2010/15(6)/066021/7/$25.00 © 2010 SPIE

Recently, we reported a new kind of light-emitting biomaterial that offers many advantages for optical hypoxia imaging[15] Iodide-substituted difluoroboron dibenzoylmethane-polylactide (BF_2dbm(I)PLA) is multiemissive, exhibiting both short-lived fluorescence (F) and long-lived phosphorescence (P) after 1- or 2-photon excitation. Especially unique is the presence of P at room temperature (and 37°C) in these PLA biomaterials, even as BNPs in aqueous environments,[16] which makes them useful for O_2 sensing via a dynamic quenching mechanism. Many pO_2 sensors are based on lifetime (τ), because τ is a concentration-independent variable, but its measurement requires specialized instrumentation not typically present in routine fluorescence detection systems. More straightforward, however, is ratiometric sensing. A simple ratio of F/P intensities at the respective emission maxima provides information about relative O_2 levels, whereas calibration allows for absolute pO_2 measurement. Ratiometric methods also eliminate the effects of concentration and fluctuations in light intensity or detector sensitivity. Previously, ratiometry had been achieved with ternary mixtures of a cyanine dye standard and an O_2-sensitive Pt porphyrin phosphor in a sol gel matrix.[17] But single-component, dual-emissive BF_2dbm(I)PLA offers the additional advantages of greater sample homogeneity, minimal dye leaching, biocompatibility, and simplified processing; because the nanoparticle serves as both the standard (F) and the oxygen sensor (P) at once, should a sensor molecule degrade, intrinsically coupled F and P are equally affected. Furthermore, long P lifetimes ($\tau = \sim 5$ ms; compare to F: $\tau = 0.5$ ns) correlate with high oxygen sensitivity, making these materials especially well suited for hypoxia imaging. The second parameter of interest is vascular oxygenation, which can be obtained using hyperspectral imaging of transmitted light through the window chamber to characterize hemoglobin absorption as a function of wavelength. From these data, it is possible to extract the hemoglobin oxygen saturation within the microvasculature, as well as the product of hemoglobin concentration and path length, which is proportional to the total attenuation through the tissue. Finally, a HIF-1 reporter construct is expressed in the 4T1 cell line used in this study, which provides a direct measure of HIF-1 activity through induced expression of GFP.[18] This enables quantification of the biologic consequences of hypoxia on an important hypoxia-associated pathway that has been shown to influence treatment resistance and tumor aggressiveness.[10]

1 Methods and Materials

1.1 *BNP Preparation*

The dye-polymer conjugate[15] BF_2dbm(I)PLA and boron nanoparticle aqueous suspensions[16] were fabricated accordingly to previously reported methods at a concentration of 1 mg/ml. Specifically, the polymer was generated by solvent-free lactide ring opening polymerization using the primary alcohol functionalized BF_2dbm(I)OH initiator and tin octoate as the catalyst. Nanoprecipitation of N,N-dimethylformamide solutions of BF_2dbm(I)PLA into water, followed by dialysis and passage through filter paper, yields nanoparticles ∼80–100 nm diam.

1.2 *Microscope*

A Zeiss MPS intravital microscope was used for all imaging, using a 2.5X objective. A DAPI excitation filter cube was used for excitation, and a liquid-crystal tunable filter was used to isolate the emission wavelengths (Varispec, Cri Inc., Woburn, MA). This filter has a 10-nm bandwidth with an electronically controllable center wavelength. A CCD camera (AM1412, Digital Video Camera Company, Austin, TX) was then used to record images. For acquisition of BNP data, the DAPI excitation filter and mercury lamp source (HBO100, Carl Zeiss AG, Oberkochen, Germany) were used to excite the sample, with the emission recorded from 425 to 575 nm in 5-nm increments using 1-s exposures. This resulted in an 31-s acquisition time for oxygen tension maps. These were acquired in increments of 7.5 min, with brightfield hemoglobin saturation acquisitions acquired continuously in-between these (GFC Mass Flow Controller, Aalborg Inc., Orangeburg, NY). This was done to minimize exposure of tissue to UV light during the hour acquisition time. For brightfield imaging used for calculation of hemoglobin saturation, an unfiltered halogen white-light source was used in transmission mode through the window, with emission recorded from 520 to 620 nm in 10-nm increments.

1.3 *BNP calibration*

The BNP solution was imaged in a 1-cm quartz cuvette with continuous bubbling of gas. The gas was a mixture of nitrogen and oxygen, with flow rates controlled by mass flow controllers (Aalborg, Inc.). The solution was initially purged of oxygen by bubbling with 100 N_2 for 30 min and then imaged using the setting described above. The oxygen flow was then incrementally increased to provide a range of oxygen concentration from 0 to 20%, with images taken at each increment after a 5-min stabilization period.

Calibration of BNP image data to absolute oxygen tension was performed as follows. First, the BNP calibration data taken from a pure BNP solution at various oxygen levels (described above) were preprocessed by normalizing them to their mean intensity. Next, they were spectrally decomposed using a two-component non-negative PARAFAC algorithm.[19] This yielded the component spectra of the fluorescence and phosphorescence emission, which can be seen in Fig. 1(a). The measured spectra of BNP emission can then be expressed as a linear combination of each of the two components using a non-negative least-squares fitting algorithm.[20] This provides the F and P component emission intensities, from which the F/P ratio was calculated. Finally, this was calibrated to absolute concentration using a second order Stern Volmer model, $F/P = a + b[O_2] + c[O_2]^2$. Figure 1(b) shows the results of this calibration, with the true oxygen concentration on the *x*-axis and the extracted oxygen concentration on the *y*-axis, shown as a boxplot. It was found that the responsiveness of the BNPs plateaus at ∼15% oxygen, with better accuracy at lower oxygen levels. The root-mean-square error on an independent testing data set was found to be 2.1 over the entire range, or 1.5 when including only oxygen levels of 15%.

1.4 *Window Chamber Model*

In vivo imaging was performed using a dorsal-skin-fold window-chamber model in a nude mouse (source, NCI Frederick).[21]

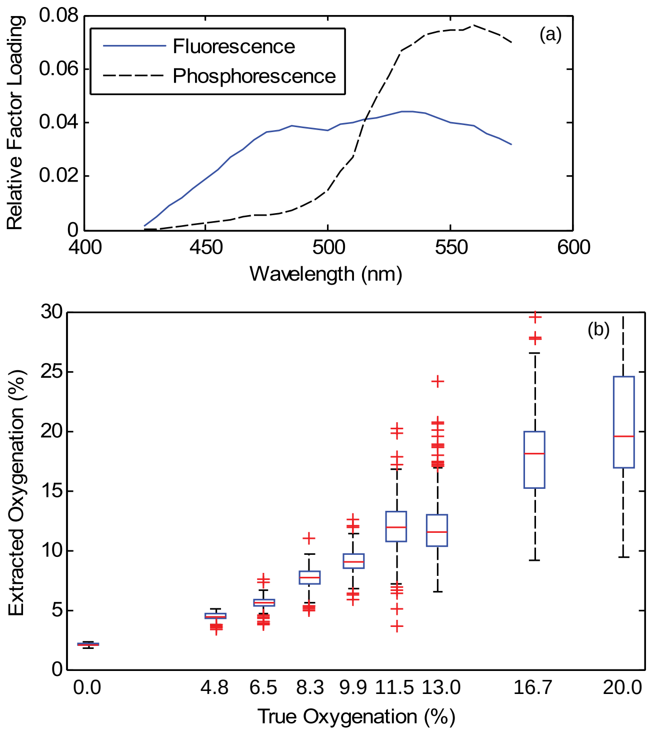

Fig. 1 Component spectra (a) are shown for fluorescence and phosphorescence emission. In addition, (b) the accuracy of extraction of the percent of oxygen is shown for the calibration data, where it can be seen that there is tight correlation at lower values, with saturation occurring at ~13% oxygen.

Briefly, this consists of a titanium metal frame that is surgically implanted onto a dorsal skin fold. The frame holds the skin taught, and one face of the skin is surgically excised, exposing the underlying skin tissue, an example of which is shown in Fig. 2. Approximately 10,000 4T1 mammary carcinoma tumor cells were injected in 20 μL of Debucco's modified eagle medium (DMEM) via a 30-gauge syringe. These cells expressed constitutive red fluorescent protein (RFP), with HIF-1 inducible GFP expression.[18] Finally, a coverglass was placed over the tumor and secured with a retaining ring. The data presented were acquired from a single mouse. All animal work was approved by Duke University's Institutional Animal Care and Use Committee.

1.5 *In Vivo Imaging*

The mouse was anesthetized using 1.5% isoflurane mixed with medical air. The animal's temperature was maintained using a heated blanket. Breathing was monitored during imaging to ensure appropriate depth of anesthesia. First, a set of background images were acquired to characterize tissue autofluorescence. Next, ~100 μL of the BNP solution was injected into the space between the window and tumor tissue to bathe the tissue, with excess fluid draining out the sides of the window, leaving a thin layer of BNP solution. Fluorescence images were acquired every 7.5 min for 1 h, with transmission images acquired continuously in-between fluorescence acquisitions.

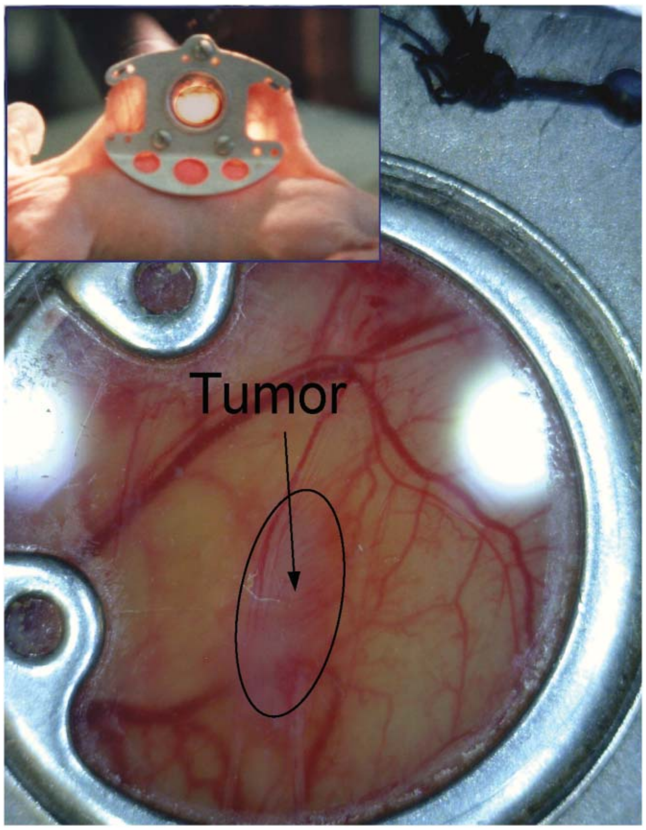

Fig. 2 The window-chamber model used in this study consists of a titanium metal frame, which holds the dorsal skin fold in place. The front skin flap is excised, and tumor cells are injected into the back plane of the opposing side skin and covered by a round coverglass. The inset shows the mouse with window implanted, with a larger view of the window itself. This is a different animal than that shown in the other figures.

1.6 *Data Processing*

Transmission images were processed using a modified form of existing techniques.[22] A modified form of Beer's law was used, which approximates attenuation through the tissue as a linear combination of absorption and scattering terms, namely

$$\log_{10}\left(\frac{I_0}{I}\right) = b_0 + b_1\mu_{\mathrm{eff}} + \sum_i \varepsilon_i C_i, \tag{1}$$

where I_0 is the transmission in the absence of tissue attenuation, which was measured using neutral density filters; b_0 is a constant term that accounts for variability in source intensity, specular reflection, or other heterogeneities in overall intensity; and μ_{eff} is the effective attenuation coefficient[23] derived from diffusion theory, $\mu_{\mathrm{eff}} = \sqrt{3\mu_a(\mu_a + \mu_s')}$, calculated for representative skin optical properties at each wavelength,[24] and accounts for attenuation due to nonhemoglobin absorption and scattering. This was empirically found to provide a good fit to the nonvascular component of attenuation in tissue (for example, in the nonvascular regions of the images). ε_i is the wavelength-dependent molar extinction coefficient of each absorber in the model, and C_i is the product of its concentration and the effective path length. In this case, two absorbers, oxygenated (HbO_2) and deoxygenated (Hb) hemoglobin, were used. The use of this approximation

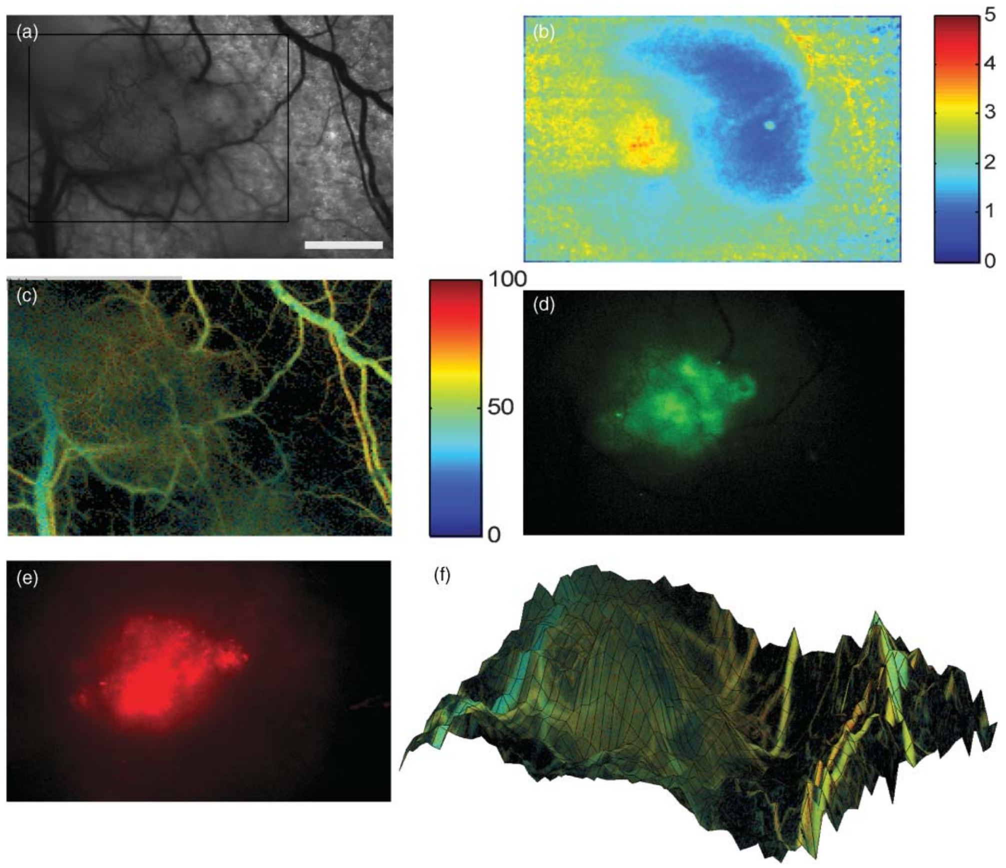

Fig. 3 (a) Bright field, (b) oxygen tension in the percent of oxygen, (c) hemoglobin oxygen saturation, (d) GFP-HIF-1 fluorescence, and (e) constitutively expressed RFP fluorescence are shown. The hemoglobin saturation (c) is shown with percent oxygen saturation on a color scale, whose brightness is modulated by the total hemoglobin content (thus, well-vascularized regions appear brighter). Also in (f), a combined plot shows the hemoglobin oxygen saturation plotted as in (c), with a 3-D projection of the tissue oxygenation shown on the vertical axis. The tumor is seen predominantly within the black box. These images were acquired toward the end of the imaging sequence ($t = 55$ min). Images are approximately 5×3.7 mm, with a 1-mm scale bar seen in (a).

enables rapid calculation of physiologic parameters, namely, hemoglobin content and saturation on a pixel-by-pixel basis. This equation is fit using a non-negative least-squares optimization algorithm over the measured wavelength range.[20] From this, the total hemoglobin content times the path length, $Hb_{tot} = C_{HbO_2} + C_{Hb}$ and the hemoglobin saturation, $Hb_{sat} = C_{HbO_2}/Hb_{tot}$ are calculated.

2 Results and Discussion

Figure 3 provides an example of optical data demonstrating quantitative imaging of tumor hypoxia and vascular function. Figure 3(a) shows a transmission image that allows for visualization of the tumor and its vasculature. Figure 3(b) depicts the oxygen tension as percent O_2 extracted from the BNP spectrum. These images reveal a region in the tumor with relatively high oxygen tension, while relatively low oxygen tension appears in the adjacent regions. This poorly oxygenated zone appears to be poorly vascularized and downstream of the tumor blood supply. Figure 3(c) shows the hemoglobin saturation on a color scale from blue (deoxygenated) to red (oxygenated). The color encoding at each pixel is then multiplied by the total hemoglobin content extracted from the same pixel, such that large vessels appear brighter, while nonvascularized pixels appear black, due to low hemoglobin content. The tumor appears well vascularized with heterogeneous oxygenation. Figure 3(d) shows the GFP intensity, normalized to the peak value, which shows distinct pockets of intense GFP fluorescence within the central part of the tumor. Figure 3(e) shows the constitutively active RFP, showing the extent of the tumor. Finally, Fig. 3(f) shows a three-dimensional (3-D) visualization of the relationship among hemoglobin oxygen saturation, hemoglobin content, and tissue oxygen tension. The hemoglobin oxygen saturation color map is overlaid on a 3-D projection of the tissue oxygen tension plotted on the surface map, with the oxygen tension appearing on the vertical axis. Thus, oxygen gradients can be visualized as slopes on the plot, with a peak appearing on one side of the tumor close to the large artery on the lower left side, with a steep fall off on the trailing edge. Video 1 shows this rendering as it appears from a variety of angles.

A key advantage of both BNP emission and hemoglobin absorption-based hyperspectral imaging techniques is their ability to monitor dynamic changes over time. To this end, the parameters described for Fig. 3 were imaged semicontinuously for the course of 1 h. This enabled characterization the temporal dynamics of each parameter and allowed for their interrelationships to be studied. Figure 4(a) shows the Spearman rank correlation between the hemoglobin saturation and tissue oxygen

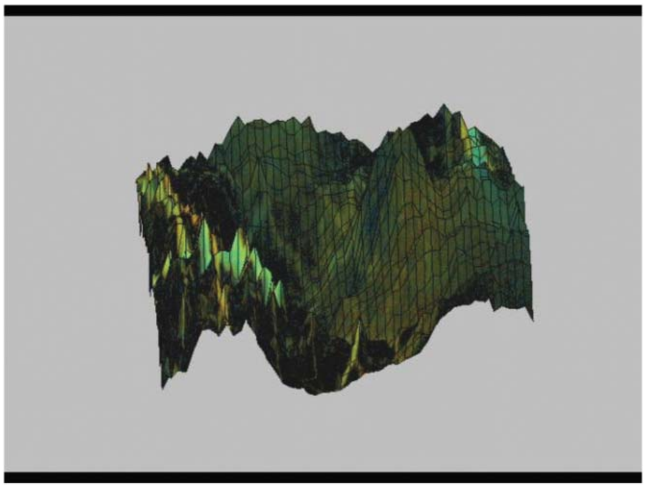

Video 1 The 3-D projection of tumor oxygen tension on the *z*-axis, along with hemoglobin saturation and total hemoglobin on the color scale identical to that shown in Fig. 3 (blue = deoxygenated → red = oxygenated, with the intensity modulated by the total hemoglobin content making vessels appear brighter). This enables visualization of gradients in tissue oxygen tension in relation to vessel morphology and oxygenation. It can be seen that the tumor oxygen tension is highly heterogeneous and has a steep gradient dividing a relatively well-oxygenated region from a relatively hypoxic region. (QuickTime, 2.6 MB). [URL: http://dx.doi.org/10.1117/1.3523363.1]

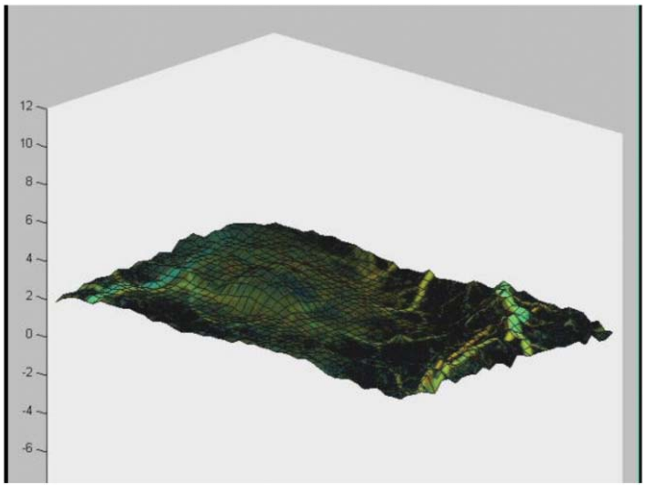

Video 2 Shows the dynamics of hemoglobin saturation and tumor oxygenation over an 1-h time period with oxygen tension shown as a 3-D projection along the *z*-axis, and hemoglobin saturation shown on a blue → red color scale identical to that in Fig. 3. Tissue oxygenation can be seen to be a dynamic process with constant variability throughout the time period. Hemoglobin saturation tracks well with changes in tissue oxygenation, with reddening vessels coinciding with increased oxygen tension. (QuickTime, 3.4 MB). [URL: http://dx.doi.org/10.1117/1.3523363.2]

tension, pixel by pixel. Solid white regions indicate areas where the hemoglobin content was not sufficient to reconstruct the hemoglobin saturation. It can be seen that there is a tight correlation of hemoglobin oxygen saturation with tumor oxygenation (median $r = 0.77$). This correlation is relatively low; however, in the central tumor region, where instable flow and shunting is expected to occur. Figure 4(b) shows the pixel-by pixel standard deviation of tissue oxygenation over time, which indicates the magnitude of oxygen fluctuations over time. It can be seen that there are two distinct regions within the tumor, with the lower left quadrant showing distinctly greater fluctuations. This region is sandwiched between the large artery and vein in the lower left quadrant. The region to the right of the tumor shows consistently lower oxygen levels throughout the imaging period, and thus has relatively low standard deviation. Video 2 shows the dynamics of tissue oxygen tension and hemoglobin saturation over time, which illustrates these trends visually. Qualitatively, it can be seen that there are often rapid changes in hemoglobin saturation (color scale), that coincide with more gradual changes in tissue oxygenation (*z*-axis height).

Finally, insofar as it is widely hypothesized that different microenvironmental phenotypes respond differently to various forms of treatment, one of the primary aims of this work was to evaluate the ability of these imaging techniques to segment tissues into different physiologic phenotypes based on the temporal dynamics of tissue oxygenation. To this end, the temporal oxygenation data were first decomposed using wavelet analysis. This is similar to Fourier analysis, which has previously been used to characterize temporal dynamics,[25] but has the advantage of being localized with respect to time as well as frequency,[26] and thus would better describe potentially abrupt or irregular changes in flow patterns. A decomposition was performed using a second-order Daubechies wavelet.[26] The discrete wavelet decomposition is applied at multiple levels, or scales. At the first level, the original signal is decomposed into an approximation and detail signal, where the detail signal is the convolution of the original signal and the wavelet function at the smallest scale or highest frequency. This essentially splits the signal into a

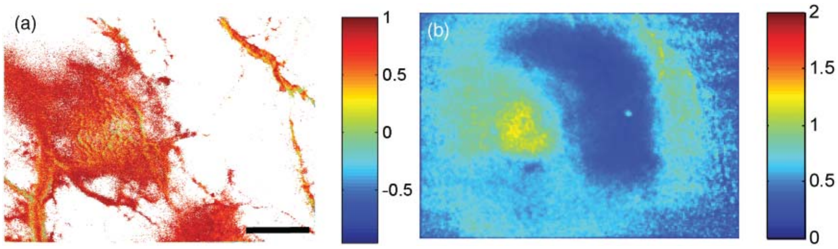

Fig. 4 (a) The Spearman rank correlation of hemoglobin oxygen saturation and tissue oxygen tension, which indicates that the central portion of the tumor has relatively low correlation between these parameters, indicating inefficiency of oxygen delivery to the tumor and possible shunting of flow. (b) The standard deviation of the tissue oxygen tension over the 1-h time period over which measurements were made, which indicates regions of the tumor that show the largest magnitude of fluctuations over time. A 1-mm scale bar is seen in (a).

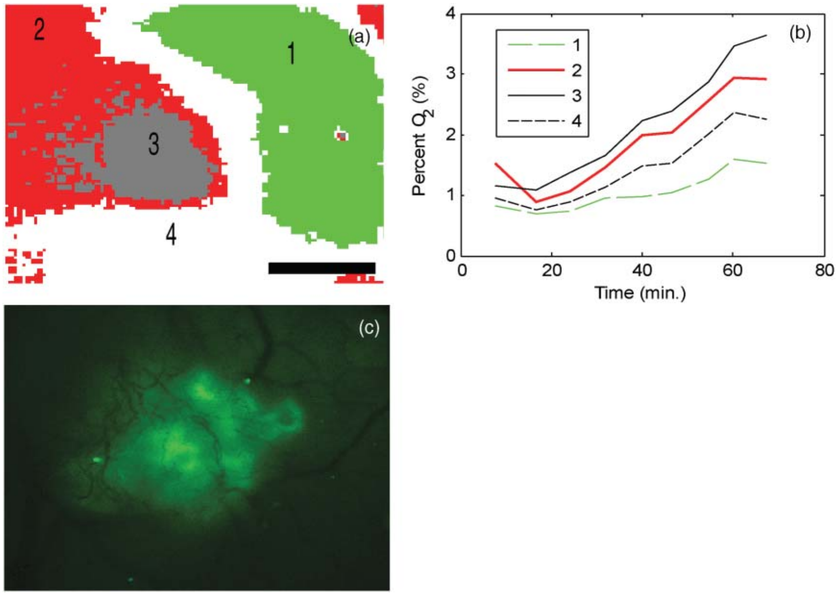

Fig. 5 Results of the clustering analysis shows (a) the spatial cluster assignment and (b) the median percent O_2 within each cluster. Also shown is the (c) HIF-1–induced GFP expression for the same tissue region. There is clear spatial segregation of the tumor and normal tissues, with the tumor being contained predominantly within clusters 2, 3, and 4. Note that this analysis was performed over a smaller region of interest indicated by the black box in Fig. 3(a). A 1-mm scale bar is seen in (a).

high-frequency component (detail) and low-frequency component (approximation), the sum of which yields the original signal. This process can be repeated with the scale of the wavelet function increasing by powers of 2 at each step, thus extracting lower and lower frequency components. In this case, a two-level decomposition was performed, which divides the temporal response into short- and long-period oscillations (center cycling periods of approximately 22.5 and 45 min). These coefficients were fed into a fuzzy c-means clustering algorithm[27] to identify which regions within and surrounding the tumor behaved most similarly over time. The fuzzy clustering algorithm classifies each tissue region according to the relative associations with each cluster centroid, allowing for the fact there is not a hard discrimination boundary between clusters; thus, cluster associations are assigned weights from 0 to 1. This was performed over a smaller region of interest containing only the tumor and immediately adjacent normal tissue as shown by the dark box in Fig. 3(a) to simplify this analysis. For the purpose of display, the maximum cluster association was selected for each pixel. Figure 5(a) shows a map of the maximum cluster association for each pixel, and Fig. 5(b) shows the median percent O_2 over time within each of these clusters. The tumor is contained predominantly within clusters 2, 3, and 4, with cluster 3 showing an earlier increase in oxygenation [see Fig. 5(b)] and also having a higher median value and larger variance over time [see Fig. 3(b)]. Interestingly, the bimodal distribution of GFP expression is also reflected in the distribution of clusters 3 and 4, which may reflect the influence of oxygen dynamics on HIF-1 activity. Specifically, cluster 3 has the largest fluctuations in oxygen tension [as seen in Figs 4(b) and 5(b), whereas cluster 4 has the lowest absolute oxygen tension [as seen in Fig. 5(b)], which have been shown to be two significant drivers of HIF-1 activity.[4] A pixel-by-pixel correlation of cluster 3 with GFP fluorescence intensity yields a Pearson correlation coefficient of 0.46 ($p < 1 \times 10^{-15}$), indicating the significant correlation between cycling hypoxia dynamics and HIF-1 activity. The remaining clusters were not correlated with GFP fluorescence (correlation coefficients ranging between -0.14 and -0.09), which may be due in part to the fact that they all include significant normal tissue regions.

One of the limitations of this study is the Beer's law assumption for tissue attenuation. This is a common practice in interpreting wide-field hyperspectral imaging data sets, but it does not account for changes in path length with respect to wavelength and optical properties, or for the heterogeneity present in tissue. We are currently developing a Monte Carlo–based approach for interpreting such data and evaluating the errors induced through use of simplified modeling techniques. Another consideration in interpreting these data is the route of administration. Because the nanoparticles were applied topically, the sensing volume is limited to the superficial tissue space. It is unclear, based on this study, whether the nanoparticles are taken up by the cells or to what extent they penetrate into the tissue, but this could influence the measurement over time as the sensing volume changes. Because epi-illumination was used, along with a relatively short imaging duration (1 h), it is likely that the measurement is highly superficial throughout the measurement time. However, these fluctuations are more likely driven by true changes in tissue oxygenation than a change in penetration depth over time, given the high correlation coefficient seen between the independent measure of hemoglobin oxygen saturation. The time scale for these fluctuations in oxygenation is consistent with those measured previously using other methods.[4,25] In the future, confocal imaging or histology could be employed to gain a better understanding of the penetration depth of these nanoparticles over time, after topical application. In addition, for many clinical applications, a topical application may not be practical. For this reason, the use of intravenous administration has also been considered and we have developed a PEGylated nanoparticle formulation that was found to accumulate near the tumor vasculature using confocal imaging.[28]

In conclusion, we have demonstrated and validated techniques by which vascular and tissue oxygenation can be imaged at high spatial and temporal resolution, enabling a detailed understanding of the tumor microenvironment and its influence on tumor gene expression. All these techniques are implemented using a simple modification to a standard fluorescent microscope, enabling a wide range of potential applications. There is no other technology that facilitates simultaneous measurement of vascular oxygen supply and tissue oxygen tension using a single instrument, and this work enables a significant advancement in our ability to characterize tissue hypoxia and its dynamic interactions *in vivo*. Hypoxia is a critical factor in a wide range of disease processes, including cancer, epilepsy, wound healing, and more. The capability of the techniques developed here to quickly, quantitatively, and nondestructively assess the dynamics of vascular oxygen supply and tissue oxygen tension could open up new possibilities for understanding of the basic mechanisms by which disease processes are influenced by hypoxia and correlating these to therapeutic response. In the future, we hope to translate these techniques to a clinical setting as a means of assessing tumor hypoxia and therapeutic response to evaluate their potential in guiding and monitoring therapy.

Acknowledgments

We thank the Department of Defense (G.M.P., Postdoctoral Fellowship Grant No. W81XWH-07-1-0355), National Institutes of Health (M.W.D., Grant No. R01CA40355), National Science Foundation (C.L.F., Grant No. CHE 0718879), and UVA Cancer Center (C.L.F., the James and Rebecca Craig Foundation and the NCI Cancer Center Support Grant No. P30 CA44579) for support for this research. We also thank the UVA NanoSTAR Institute for supporting our early efforts to develop and test BNPs as biomedical imaging agents. C.L.F. has financial interest in Luminesco, Inc., which is commercializing the BNP technology. Also thanks to Dr. Siqing Shan for providing Fig. 2.

References

1. G. Lorusso and C. Rugg, "The tumor microenvironment and its contribution to tumor evolution toward metastasis," *Histochem. Cell Biol.* **130**(6), 1091–1103 (2008).
2. P. Vaupel, "Tumor microenvironmental physiology and its implications for radiation oncology," *Semin. Radiat. Oncol.* **14**(3), 198–206 (2004).
3. K. J. Williams, R. L. Cowen, and I. J. Stratford, "Hypoxia and oxidative stress in breast cancer—tumour hypoxia: therapeutic considerations," *Breast Cancer Res.* **3**(5), 328–331 (2001).
4. M. Dewhirst, "Relationships between cycling hypoxia, HIF-1, angiogenesis and oxidative stress," *Radiat. Res.* **172**(6), 653–665 (2009).
5. R. G. Bristow and R. P. Hill, "Hypoxia and metabolism: hypoxia, DNA repair and genetic instability," *Nat. Rev. Cancer.* **8**(3), 180–192 (2008).
6. J. M. Brown, "Evidence for acutely hypoxic cells in mouse tumours, and a possible mechanism of reoxygenation," *Br. J. Radiol.* **52**(620), 650–656 (1979).
7. P. Martinive, F. Defresne, C. Bouzin, J. Saliez, F. Lair, V. Gregoire, C. Michiels, C. Dessy, and O. Feron, "Preconditioning of the tumor vasculature and tumor cells by intermittent hypoxia: implications for anticancer therapies," *Cancer Res.* **66**(24), 11736–11744 (2006).
8. P. Martinive, F. Defresne, E. Quaghebeur, G. Daneau, N. Crokart, V. Gregoire, B. Gallez, C. Dessy, and O. Feron, "Impact of cyclic hypoxia on HIF-1alpha regulation in endothelial cells—new insights for anti-tumor treatments," *FEBS J.* **276**(2), 509–518 (2009).
9. M. W. Dewhirst, "Intermittent hypoxia furthers the rationale for hypoxia-inducible factor-1 targeting," *Cancer Res.* **67**(3), 854–855 (2007).
10. M. Dewhirst, Y. Cao, and B. Moeller, "Cycling hypoxia and free radicals regulate angiogenesis and radiotherapy response," *Nat. Rev. Cancer* **8**(6), 425–437 (2008).
11. R. K. Jain, "Normalization of tumor vasculature: an emerging concept in antiangiogenic therapy," *Science* **307**(5706), 58–62 (2005).
12. R. Springett and H. Swartz, "Measurements of oxygen in vivo: overview and perspectives on methods to measure oxygen within cells and tissues," *Antioxid. Redox Signal* **9**(8), 1295–1301 (2007).
13. M. W. Dewhirst, B. Klitzman, R. D. Braun, D. M. Brizel, Z. A. Haroon, and T. W. Secomb, "Review of methods used to study oxygen transport at the microcirculatory level," *Int. J. Cancer* **90**(5), 237–255 (2000).
14. A. R. Padhani, K. A. Krohn, J. S. Lewis, and M. Alber, "Imaging oxygenation of human tumours," *Eur. Radiol.* **17**(4), 861–872 (2007).
15. G. Zhang, G. M. Palmer, M. W. Dewhirst, and C. L. Fraser, "A dual-emissive-materials design concept enables tumour hypoxia imaging," *Nat. Mater.* **8**(9), 747–751 (2009).
16. A. Pfister, G. Zhang, J. Zareno, A. F. Horwitz, and C. L. Fraser, "Boron polylactide nanoparticles exhibiting fluorescence and phosphorescence in aqueous medium," *ACS Nano.* **2**(6), 1252–1258 (2008).
17. Y. E. L. Koo, Y. F. Cao, R. Kopelman, S. M. Koo, M. Brasuel, and M. A. Philbert, "Real-time measurements of dissolved oxygen inside live cells by organically modified silicate fluorescent nanosensors," *Anal. Chem.* **76**(9), 2498–2505 (2004).
18. B. J. Moeller, Y. Cao, C. Y. Li, and M. W. Dewhirst, "Radiation activates HIF-1 to regulate vascular radiosensitivity in tumors: role of reoxygenation, free radicals, and stress granules," *Cancer Cell* **5**(5), 429–441 (2004).
19. C. Andersson and R. Bro, "The N-way Toolbox for MATLAB," *Chemom. Intell. Lab. Syst.* **52**(1), 1–4 (2000).
20. R. Bro and S. DeJong, "A fast non-negativity-constrained least squares algorithm," *J. Chemom.* **11**(5), 393–401 (1997).
21. Q. Huang, S. Shan, R. D. Braun, J. Lanzen, G. Anyrhambatla, G. Kong, M. Borelli, P. Corry, M. W. Dewhirst, and C. Y. Li, "Noninvasive visualization of tumors in rodent dorsal skin window chambers," *Nat. Biotechnol.* **17**(10), 1033–1035 (1999).
22. B. S. Sorg, B. J. Moeller, O. Donovan, Y. Cao, and M. W. Dewhirst, "Hyperspectral imaging of hemoglobin saturation in tumor microvasculature and tumor hypoxia development," *J. Biomed. Opt.* **10**(4), 44004 (2005).
23. R. Splinter and B. A. Hooper, *An introduction to biomedical optics*, Taylor & Francis, New York (2007).
24. R. Huang and S. Jacques, "Skin optics summary" (1998); http://omlc.ogi.edu/news/jan98/skinoptics.html.
25. L. I. Cardenas-Navia, D. Mace, R. A. Richardson, D. F. Wilson, S. Shan, and M. W. Dewhirst, "The pervasive presence of fluctuating oxygenation in tumors," *Cancer Res.* **68**(14), 5812–5819 (2008).
26. J. S. Walker, *A primer on wavelets and their scientific applications*, Chapman & Hall/CRC, Boca Raton (2008).
27. F. Höppner, *Fuzzy cluster analysis : methods for classification, data analysis, and image recognition*, Wiley, Hoboken, NJ (1999).
28. F. Kersey, G. Zhang, G. Palmer, M. Dewhirst, and C. Fraser, "Stereocomplexed poly(lactic acid)-poly(ethylene glycol) nanoparticles with dual-emissive boron dyes for tumor accumulation," *ACS Nano.* (2010).